Metasomatism induced by alkaline magma in the upper mantle of northern Victoria Land (Antarctica): an experimental approach

C. Perinelli, A. Orlando, A. M. Conte, P. Armienti, D. Borrini, B. Faccini and V. Misiti

Geological Society, London, Special Publications 2008; v. 293; p. 279-302
doi:10.1144/SP293.13

Metasomatism induced by alkaline magma in the upper mantle of northern Victoria Land (Antarctica): an experimental approach

C. PERINELLI[1], A. ORLANDO[2], A. M. CONTE[3], P. ARMIENTI[1], D. BORRINI[4], B. FACCINI[5] & V. MISITI[6]

[1]*Dipartimento di Scienze della Terra, Università di Pisa, via S. Maria 53, 56100 Pisa, Italy (e-mail: cperinelli@dst.unipi.it)*

[2]*CNR–IGG, UO di Firenze, via G. La Pira, 4, 50121 Firenze, Italy*

[3]*CNR–IGG, UO di Roma, p.le Aldo Moro 5, 00185 Roma, Italy*

[4]*Dipartimento di Scienze della Terra, Università di Firenze, via G. La Pira, 4, 50121 Firenze, Italy*

[5]*Dipartimento di Scienze della Terra, Università di Ferrara, via Saragat 1, 44100 Ferrara, Italy*

[6]*INGV Sezione di Sismologia e Tettonofisica, via di Vigna Murata 605, 00143 Roma, Italy*

Abstract: Magma generation in the Ross Sea system is related to partial melting of strongly metasomatized mantle sources where amphibole most probably plays a crucial role. In this context, metasomatism induced by a mela-nephelinite melt in lithospheric mantle of the Mt. Melbourne Volcanic Province (northern Victoria Land (NVL), Antarctica) was investigated experimentally studying the effects of melt interaction with lherzolite at 1.5–2.0 GPa and $T = 975–1300\ ^{\circ}C$, and wehrlite at 1.0 GPa and $T = 1050–1250\ ^{\circ}C$. The experiments were designed to induce melt infiltration into the ultramafic rocks. The observed modifications in minerals are compared with those found in mantle xenoliths from NVL. The effects of metasomatic modifications are evaluated on the basis of run temperature, distance from the infiltrating melt and the diffusion rates of chemical components. Both in lherzolite and wehrlite, clinopyroxene exhibits large compositional variations ranging from primary diopside to high-Mg–Cr–(Na) augitic and omphacitic clinopyroxenes in lherzolite, and to low-Mg and high-Ti–Al–Fe–Na augites in wehrlite. Olivine (in wehrlite) and spinel (in lherzolite) are also compositionally modified: the former shows enrichment in Fe and the latter displays a higher Cr/(Cr + Al) ratio. The systematic variations in mineral compositions imply modifications of the chemistry of the infiltrating melt as recorded by the glass veinlets and patches observed in some charges. In experiments involving wehrlite paragenesis, the glass composition approaches that of melt patches associated with both amphibole-free and amphibole-bearing natural samples, and is related to olivine + clinopyroxene crystallization coupled with primary clinopyroxene dissolution at the contact between the metasomatizing melt and the solid matrix. Even if amphibole crystallization was not attained in the experiments, we were able to explain the occurrence of amphibole in the natural system considering that in this case a hot metasomatizing melt infiltrates a cooler matrix.

The Ross rift system and accompanying Cenozoic volcanism of the Mt. Melbourne Volcanic Province (northern Victoria Land (NVL), Antarctica) has been related either to the occurrence of a long-lasting mantle plume or to the top-down control of the tensile state of the lithosphere (Rocholl *et al.* 1995; Rocchi *et al.* 2006). Alkali-basaltic eruptions brought to the surface abundant mantle xenoliths, mainly represented by both amphibole-free and amphibole-bearing spinel peridotites and cumulitic pyroxenites–wehrlites, which can provide information on the thermal state and the chemical and mineralogical composition of lithospheric mantle.

Previous studies have revealed a significant mineralogical and compositional heterogeneity of NVL upper mantle, as a result of the combined effects of partial melting and both modal and cryptic metasomatic processes (Coltorti *et al.* 2004, 2006; Perinelli *et al.* 2006). Modal metasomatism of NVL mantle xenoliths is recognizable by the occurrence of pargasitic to kaersutitic amphibole, usually associated with glass. Amphibole may form veins or grow as disseminated grains around clinopyroxene and/or spinel. Disseminated and vein amphiboles have similar major and trace element composition and their genesis

From: COLTORTI, M. & GRÉGOIRE, M. (eds) *Metasomatism in Oceanic and Continental Lithospheric Mantle.* Geological Society, London, Special Publications, **293**, 279–302.
DOI: 10.1144/SP293.13 0305-8719/08/$15.00

is attributed to the reaction of lherzolitic rocks with an infiltrating magma, possibly an undersaturated, TiO_2-rich Na alkaline silicate melt (Coltorti *et al.* 2004). According to Coltorti *et al.* the reaction that generates amphibole first produces progressive modifications on primary mantle paragenesis forming secondary olivine (ol2-nat), clinopyroxene (cpx-A) and spinel (sp2-nat), and consuming orthopyroxene. These neoformed phases represent 'precursors' of amphibole as well as being associated with it. Coltorti *et al.* (2004) inferred that the possible metasomatic agent was similar to the most undersaturated rock found in the province, a nephelinite cropping out at Greene Point (sample SAX20, Orlando *et al.* 1997; Perinelli *et al.* 2006). An analogous nephelinitic melt has been considered by Perinelli & Armienti (2005) to be responsible for the metasomatic events recognized in wehrlites and pyroxenites cropping out in the same area.

The concurrent presence of amphibole-free and amphibole-bearing spinel peridotites and pyroxenites has been documented in several areas worldwide (Xu & Bodinier 2004, and references therein). They may result from the same metasomatic event (Xu & Bodinier 2004) but are related to two different mechanisms: (1) 'wall-rock' metasomatism, caused by the transport of melt in fractures (veins and dykes); (2) 'diffuse' metasomatism related to percolation of small melt fractions along grain boundaries in a solid matrix. The differences in metasomatic assemblage and mineral compositions (major and trace elements) in the xenoliths can be explained by the P–T control on amphibole stability and the progressive chemical variation of infiltrating melts (Xu & Bodinier 2004).

Despite the interest in completely highlighting how 'diffuse' and/or 'wall-rock' metasomatism acts, few experimental studies on interaction of alkaline melts with mantle rocks have been undertaken (e.g. Sen & Dunn 1994; Shaw *et al.* 1998; Rapp *et al.* 1999; Shaw 1999). Therefore, to better understand the processes involved in the metasomatism in NVL mantle, a series of high-pressure–high-temperature experiments were performed to simulate *in situ* the effect of different extents of metasomatism. In particular, the aim of the experiments was to investigate the reactions affecting lherzolite or wehrlite phases during interaction with alkaline melts, and to test the possibility that ensuing reactions generate amphibole.

The experiments were performed at pressure conditions of 1.5–2.0 GPa for lherzolite and 1.0 GPa for wehrlite in a P–T range close to the conditions of metasomatism that may have occurred in nature, according to Perinelli *et al.* (2006).

Starting materials

Nephelinite–lherzolite runs at high T ($>1100\ ^\circ$C)

In these runs we used fine-grained ($<100\ \mu$m) nephelinite SAX20 (sampled at Greene Point) containing olivine phenocrysts (Fo_{71-78}) (Table 1) in a groundmass of diopsidic clinopyroxene, feldspar ($Ab_{49}Or_{47}An_4$), nepheline ($Ne_{66-70}Ks_{3-6}Qtz_{23-30}$) and spinel (magnetite$_6$–ulvöspinel$_{94}$ series).

Anhydrous lherzolite ($<50\ \mu$m) from a xenolith (sample 154L, provided by M. Coltorti) was chosen as representative of unmetasomatized mantle. Mineral compositions are given in Table 1.

Nephelinite–lherzolite runs at low T ($<1100\ ^\circ$C)

In these runs we used the 154 L lherzolite and a SAX20 glass_5bru glass obtained melting in air SAX20 powder at 1400 °C (quenched after 2 min) in a Deltech DT-31VT-OS2 vertical quench furnace and remelting the resulting glass at the same temperaure, after grinding. Natural brucite ($Mg(OH)_2$) powder (5 wt%, 99.9% pure) was added to the (anhydrous) glass, as its decomposition at run conditions (Irving *et al.* 1977) supplies water to the system (Table 1). Moreover, another glass (SAX20-2.5TiO_2glass_5bru) was prepared by adding 2.5 wt% TiO_2 to SAX20 prior to the two melting cycles at 1400 °C; as in the preparation of the previous starting material, 5 wt% of 99.9% pure brucite was added to the mixture before loading the capsule.

MgO and TiO_2 additions allow the bulk composition of the glass to approach that of metasomatic melts inferred by Coltorti *et al.* (2004) (Table 1) and water released by brucite enhances reaction rates and counterbalances the water loss during glass synthesis.

Nephelinite–wehrlite runs

Nephelinite SAX20 was used with a fresh wehrlite (BRP19), free of any metasomatic feature, sampled at Browning Pass, on the coast of Ross Sea, NVL. This rock consists of *c.* 50% olivine (Fo_{81}), *c.* 50% diopsidic clinopyroxene and a trace of Cr-spinel (Table 1).

Experimental and analytical procedures

Nephelinite–lherzolite runs

At $T > 1100\ ^\circ$C nephelinite powder was placed at the bottom of a graphite capsule, to avoid Fe loss,

Table 1. *Representative composition of minerals in lherzolite and in wehrlite together with whole-rock composition of nephelinite SAX20 and other synthetic starting materials used in the runs. Metasomatizing melts inferred by Coltorti et al. (2004) are also reported for comparison*

	Lherzolite 154L				Wehrlite BRP19			SAX20*	SAX20glass_5bru nominal	SAX20-2.5TiO_2glass_5bru nominal	melt1†	melt2†
	ol1	opx1	cpx1	sp1	ol1	cpx1	sp1					
SiO_2	40.73	55.93	52.81	bdl	40.55	51.18	0.05	40.78	39.19	38.23	39.68	47.74
TiO_2	bdl	bdl	0.07	0.01	bdl	0.67	2.18	3.62	3.48	5.74	7.48	5.66
Al_2O_3	bdl	3.25	3.19	48.04	bdl	4.16	26.84	11.81	11.35	11.07	12.13	10.49
FeO^T	8.79	5.59	1.93	11.32	17.57	6.01	28.53	14.50	13.93	13.59	3.74	5.66
MnO	0.09	0.18	0.14	0.02	0.19	0.10	0.10	0.28	0.27	0.26		
MgO	50.20	34.17	16.99	18.49	41.53	16.43	11.42	9.33	12.26	12.04	17.91	13.32
CaO	0.02	0.55	23.56	bdl	0.18	19.75	bdl	9.23	8.87	8.65	14.96	9.9
Na_2O	n.d.	0.04	0.39	n.d.	n.d.	0.64	n.d.	5.31	5.10	4.98	4.04	4.01
K_2O	bdl	bdl	bdl	bdl	bdl	bdl	bdl	1.54	1.48	1.44		2.83
Cr_2O_3	bdl	0.66	0.79	20.76	bdl	0.92	29.99	0.08	0.08	0.08		
NiO	0.40	n.d.	n.d.	n.d.	bdl	bdl	bdl	0.03	0.03	0.03		
P_2O_5	n.d.	n.d.	n.d.	n.d.	n.d.	n.d.	n.d.	1.60	1.54	1.50		
H_2O	n.d.	n.d.	n.d.	n.d.	n.d.	n.d.	n.d.	0.90	1.47	1.47		
Total	100.23	100.37	99.87	98.64	100.02	99.86	99.11	99.01	99.05	99.08	99.94	99.61
Fo	91.05				80.81							
En		90.38	48.44			48.26						
Fs		8.57	3.31			10.07						
Mg-no.				0.75			0.50					
Cr-no.				0.22			0.43					

ol1, olivine; opx1, orthopyroxene; cpx1, clinopyroxene; sp1, spinel; H_2O value refers to LOI. bdl, below detection limit; n.d., not determined; Fo, En, Fs, forsteritic, enstatitic, ferrosilitic components, respectively; Mg-number = $Mg/(Mg + Fe^{2+})$; Cr-number = $Cr/(Cr + Al)$.

*From Orlando *et al*. (1997).

†Metasomatizing melts from Coltorti *et al*. (2004).

and in close contact with lherzolite powder; the nephelinite/lherzolite ratio was *c.*1 in all runs. The graphite capsule (4 mm long) was then inserted into an outer Pt capsule (o.d. 3.0 mm, i.d. 2.8 mm, length *c.* 7–8 mm), which was welded shut. Experiments were performed at 1.5 and 2.0 GPa, at temperatures in the range 1150–1300 °C; runs lasted up to 95 h. No H_2O was added to the charges.

$Ag_{50}Pd_{50}$ capsules were used in runs at $T < 1100$ °C. The melt–peridotite couples were assembled as sandwiches of lherzolite between either SAX20glass_5bru or SAX20-2.5TiO_2-glass_5bru powders, again with a melt/lherzolite ratio of *c.* 1. Because of the lower temperatures of these experiments, longer durations (190–212 h) were used.

All of these experiments (Table 2) were carried out in a $\frac{1}{2}$ inch piston-cylinder apparatus (at CNR–IGG HP–HT Laboratory, Florence) using a salt–Pyrex–crushable alumina assembly and the 'hot piston-out' technique. Pressure was calibrated using the reaction ferrosilite = fayalite + quartz at 1000 °C (Bohlen *et al.* 1980). Further experimental details have been given by Orlando & Borrini (2001). Temperature was measured by a Pt_{100}–$Pt_{90}Rh_{10}$ thermocouple and no correction for the effect of pressure was applied to the thermocouple e.m.f. The pressure was considered accurate to ±0.05 GPa and temperature to ±5 °C of stated values.

Oxygen fugacity during the experiments at $T > 1100$ °C was estimated according to the calculated Fe^{3+} in spinel coexisting with olivine and orthopyroxene (Ballhaus *et al.* 1990) and the C–COH buffer (Ulmer & Luth 1991). The two independent estimates are consistent, and give values of $\Delta FMQ < -1.2$ (where FMQ is the fayalite –magnetite–quartz buffer).

Run products were analysed on a JEOL JXA-8600 electron microprobe operated at 15 kV accelerating voltage and 10 nA beam current. Count times ranged from 10 to 40 s (same times for backgrounds) and alkali loss was minimized by defocusing the electron beam to 15 μm. Data were corrected for the matrix effect using the Bence & Albee (1968) method and errors were estimated according to Vaggelli *et al.* (1999).

Nephelinite–wehrlite runs

These samples were prepared by packing a layer of wehrlite powder over a layer of nephelinite powder in a graphite capsule, to obtain a wehrlite/nephelinite ratio of *c.* 1 in all charges. The graphite capsule was put into a Pt capsule, stored in an oven at 110 °C overnight to remove humidity, and then welded shut. The final length of capsules was 8–9 mm.

All nephelinite–wehrlite experiments were run in a 3/4 inch piston-cylinder apparatus, at the HP–HT Laboratory of Experimental Volcanology and Geophysics of Istituto Nazionale di Geofisica e Vulcanologia (INGV), Rome.

Experiments were performed at 1.0 GPa at 1250–1050 °C; run times were in the range 5–48 h (Table 2). Experiments performed at 1150 °C and 1050 °C were repeated with *c.* 3%water in the capsules. Below we identify as 'hydrous' the experiments with H_2O added in the charge and 'anhydrous' the runs without H_2O addition, although in the latter experiments water is present because of its occurrence in nephelinite (Table 1).

The pressure cell consists of an assembly of NaCl–Pyrex, with a graphite heater and magnesia inner sleeves. The dimensions of this assembly allowed volatile-free and volatile-added charges to be run at the same time. Al_2O_3 (anhydrous runs) or pyrophyllite (water-bearing runs) powder was packed around the capsules (Freda *et al.* 2001). The temperature was controlled by a $W_{95}Re_5$–$W_{74}Re_{26}$ (type C) thermocouple. The thermocouple tip was placed in the middle of *c.* 10 mm long hotspot between the two capsules (for further details see Misiti *et al.* 2006). The thermocouple was encapsulated in an Al_2O_3 sleeve. The temperature was considered accurate to ±3 °C of stated values.

Pressure was calibrated against the NaCl melting point (Bohlen *et al.* 1980) at 1004 °C at 1.0 GPa and 1090 °C at 1.5 GPa. Pressure correction was +250 bar.

Experiments were first pressurized to the target pressure and then heated at a rate of 200 °C min^{-1} to 20 °C below the target temperature. A slower rate of 40 °C min^{-1} was applied within the last 20 °C of heating to avoid overshooting. The experiment was ended by switching off the heating power while maintaining pressure constant. The initial quench rate was about 2000 °C min^{-1}. The pressure is considered accurate to ±0.05 GPa and possible pressure effects on the e.m.f. of the thermocouple were ignored.

Oxygen fugacity estimated according to Ulmer & Luth (1991) is for all experiments $\Delta FMQ < -1.3$. Experimental conditions and results are summarized in Table 2.

Back-scattered electron (BSE) images of nephelinite–wehrlite runs were collected at the Dipartimento di Scienze della Terra of Pisa University, using a Philips XL30 SEM.

Microanalyses of phase composition were performed on polished carbon-coated mounts by a four-spectrometer Cameca SX50-52 electron microprobe using a 15 keV accelerating voltage, a 15 nA beam current (at CNR–IGAG, Rome).

Table 2. *Experimental assemblage, run conditions and results*

Run	Starting material	Capsule	*P* (GPa)	*T* (°C)	Duration (h)	Detected phases
169	154L SAX20	C–Pt	1.5	1150	3	*lh*: ol1, opx1, cpx1, sp1, cpx2, sp2 *nf*: glass, cpx, ol, sp, ne
167	154L SAX20	C–Pt	1.5	1200	4	*lh*: ol1, opx1, cpx1, sp1, cpx2, sp2 *nf*: glass, cpx, ol, sp
170	154L SAX20	C–Pt	1.5	1250	49	*lh*: ol1, opx1, cpx1, sp1, cpx2, sp2, <<glass *nf*: glass, cpx, ol
166	154L SAX20	C–Pt	1.5	1300	75	*lh*: ol1, opx1, cpx1, sp1, cpx2, sp2, <<glass *nf*: glass
173	154L SAX20	C–Pt	2.0	1300	95	*lh*: ol1, opx1, cpx1, sp1, cpx2, sp2 *nf*: glass, cpx, ol, rhönite, sp
178	*154L* *SAX20-2.5TiO$_2$glass_5bru*	$Ag_{50}Pd_{50}$	2.0	975	212	*lh*: ol1, opx1, cpx1, sp1, cpx2, sp2 *nf*: glass, ol, cpx, sp
177	*154L* *SAX20-2.5TiO$_2$glass_5bru*	$Ag_{50}Pd_{50}$	2.0	1025	190	*lh*: ol1, opx1, cpx1, sp1, (ol2), (opx2), cpx2, sp2, <glass2 *nf*: glass, oxides, cpx, ap
176	*154L* *SAX20glass_5bru*	$Ag_{50}Pd_{50}$	2.0	1025	190	*lh*: ol1, opx1, cpx1, sp1, (ol2), (opx2), cpx2, sp2, <glass2 *nf*: glass, ol, cpx, rhönite, ap
141	BRP19 SAX20	C–Pt	1.0	1250	5	*py*: ol1, cpx1, ol2, cpx2, glass *nf*: glass
140	BRP19 SAX20	C–Pt	1.0	1200	8	*py*: ol1, cpx1, ol2, cpx2, <glass *nf*: glass, ol
144	BRP19 SAX20	C–Pt	1.0	1175	8	*py*: ol1, cpx1, ol2, cpx2, <glass *nf*: glass, ol
150	BRP19 SAX20	C–Pt	1.0	1150	8	*py*: ol1, cpx1, ol2, cpx2, <glass *nf*: glass, ol, cpx, oxides
153	BRP19 SAX20	C–Pt	1.0	1150	24	*py*: ol1, cpx1, ol2, cpx2, glass *nf*: glass, ol, cpx, oxides
154	BRP19 SAX20	C–Pt	1.0	1050	48	*py*: ol1, cpx1, ol2, cpx2, glass *nf*: glass, ol, cpx, oxides, ne
153*	BRP19 SAX20	C–Pt	1.0	1150	24	*py*: ol1, cpx1, ol2, cpx2, glass *nf*: glass, ol, cpx, oxides
154*	BRP19 SAX20	C–Pt	1.0	1050	48	*py*: ol1, cpx1, ol2, cpx2, glass, < sp2 *nf*: glass, ol, cpx, oxides, rhönite, ap

C–Pt, double capsules with graphite inside Pt; *lh*, *nf*, *py* in the *Detected phases* column refer to phases found in lherzolitic, nephelinitic and pyroxenitic portions of the capsule, respectively; ol, olivine; opx, orthopyroxene; cpx, clinopyroxene; sp, spinel; ap, apatite; ne, nepheline; suffixes *1* and *2* refer to original and neo-formed phases, respectively; <, scarce; ≪, rare.
*Experiments with *c*. 3 wt% H_2O added in the charge.

Matrix effect corrections (ZAF) were performed using the algorithm of Philibert (1963) and Duncumb & Reed (1968). A focused beam was used for minerals, whereas glasses were analysed with a 10 μm diameter beam to minimize volatilization of sodium; a 5 μm diameter beam was used for small volumes of glass in the lowest-temperature experiments.

Results

Nephelinite–lherzolite runs

Phases detected in experimental products are reported in Table 2 and chemical analyses of lherzolite are shown in Tables 3–5. In experimental runs glass is seldom found in lherzolite and is not related to the distance from the lherzolite–nephelinite interface or to the occurrence and the composition of neoformed phases (see below).

Runs at high T (>1100 °C). Nephelinite was completely molten at 1.5 GPa and 1300 °C. At lower temperatures it was partially molten and clinopyroxene + olivine, spinel and nepheline progressively saturated the liquid at decreasing temperature. In the run at 2.0 GPa glass coexisted with clinopyroxene, olivine, spinel and rhönite (Table 2).

The lherzolite area of the charges contains small, rare glass pockets (mostly not analysable by electron microprobe) with the exception of the run performed at the lowest temperature (Fig. 1a).

In the lherzolitic portion of the capsules at 1250 °C, some glass analyses attain a SiO_2-rich latitic composition; the original phases, olivine (ol1), clinopyroxene (cpx1), orthopyroxene (opx1) and spinel (sp1) are accompanied by scattered neoformed subhedral clinopyroxene (cpx2, Fig. 1a) and spinel (sp2). Analyses of neoformed phases in the lherzolitic portion of the charges are reported in Tables 3–5.

At 1.5 GPa, cpx2 is augite in all the runs. With respect to the original phases, there are increases in MgO (from 16.5–17.4 to 26 wt%), Na_2O (from 0.4–0.8 to 2.2 wt%) and Cr_2O_3 (from 0.4–0.9 to 2.7 wt%), whereas CaO decreases (from 22.6–23.8 to 7.6 wt%). In particular, in the run carried out at 1150 °C neoformed clinopyroxene is mainly found around orthopyroxene crystals together with glass that is not analysable (Fig. 1b).

At 2.0 GPa cpx2 has a higher Na_2O content (2.3–4.1 wt%) than cpx2 synthesized at 1.5 GPa; the CaO content is generally low (9.7–14.2 wt%) and Cr_2O_3 and MgO content are in the range of 1.2–1.8 and 17.4–18.4 wt%, respectively. According to the Morimoto (1989) classification, most of the analysed crystals are omphacite. Neoformed spinel (sp2) occurs as subhedral crystals or coronas around original crystals in all the runs, as shown in Figure 1c. Sp2 crystals generally show higher Cr-number ($Cr/(Cr + Al)$; up to 0.85) and lower Mg-number ($Mg/(Mg + Fe^{2+})$; down to 0.63) with respect to sp1 crystals. The highest Cr_2O_3 content (67.2 wt%) was found in experiments at 1150 °C.

Runs at low T (<1100 °C). BSE images reveal that some olivine crystals close to the lower interface sank into the nephelinitic portion and reacted from Fo_{90} to Fo_{85}. In these runs interaction occurred despite the low temperature, probably because of the reactivity of glass as starting material and the long durations utilized (190–212 h).

In the run with SAX20glass_5bru, in the nephelinitic portions of the capsule, glass is dominant and olivine (Fo_{78}), augitic clinopyroxene, rhönite and apatite crystals are commonly found. In the lherzolite, neoformed phases join the original ones: olivine crystals equilibrated to Fo_{86} close to the lower interface (ol2) and small (<20 μm) enstatitic orthopyroxene crystals (opx2) enriched in Na_2O (0.5–1.4 wt%) and CaO (1.1–1.6 wt%) relative to opx1 are sometimes found scattered in sporadic glass patches along the capsule walls. Glass analyses show very low totals (<70 wt%), probably because of the combined effect of water content and poorly polished surfaces of micro-vesicular or friable glass (e.g. see Peterson & Newton 1990). Neoformed augite and omphacite, enriched in Na_2O (up to 3.3 wt%) and Cr_2O_3 (up to 2.5 wt%) and depleted in CaO (16.2–19.8 wt%) with respect to cpx1, are found throughout the lherzolitic portion together with high Cr-number (0.39–0.54)–low Mg-number (0.59–0.60) neoformed spinel.

In runs with SAX20-2.5TiO_2glass_5bru (Ti-doped), at 1025 °C, glass is the dominant phase in the nephelinitic portions of the charge; however, small (<10 μm) ilmenite–hematite crystals are scattered in the glass together with scarce clinopyroxene and apatite. As in the undoped run, we detected in the peridotite high-Na_2O and -CaO orthopyroxene (opx2) in (nephelinitic) glass pockets and high-Na_2O, -Cr_2O_3 and low-CaO neoformed augitic and omphacitic clinopyroxene. High Cr-number (0.64–0.65) spinels (sp2) are commonly present throughout the lherzolitic portion; their TiO_2 contents (1.2–1.8 wt%) are greater than in sp1 and in sp2 of the undoped run. Furthermore, the Mg-number (0.48–0.50) is the lowest among the analysed spinels in all experiments.

At 975 °C some clinopyroxene, olivine and spinel crystals are scattered in the glass in the nephelinitic portions of the capsule. Some olivine (Fo_{90}) crystals, probably from the lherzolitic portion, are present in the lower nephelinitic

Table 3. *Representative electron microprobe analyses of cpx2 in lherzolite*

Run	169	169	169	167	167	167	167	167	170	170	166	
P (GPa)/T (°C)	1.5/1150	1.5/1150	1.5/1150	1.5/1200	1.5/1200	1.5/1200	1.5/1200	1.5/1200	1.5/1250	1.5/1250	1.5/1300	
SiO_2	54.59	54.29	53.51	47.67	53.39	53.97	54.10	54.19	54.31	54.34	53.27	
TiO_2	bdl	bdl	0.11	2.35	0.17	0.18	0.41	0.03	0.18	0.20	0.09	
Al_2O_3	0.71	0.70	1.94	8.82	3.98	4.06	4.49	2.96	3.24	4.92	3.23	
Cr_2O_3	1.91	1.47	0.83	0.81	1.93	1.82	0.86	1.85	1.20	2.71	1.77	
FeO^T	2.44	2.58	3.18	7.39	5.59	5.54	6.21	5.73	4.28	3.24	3.57	
MnO	0.32	0.14	bdl	0.22	0.08	0.17	0.28	0.30	0.28	0.23	0.11	
MgO	19.42	19.19	19.29	14.02	22.63	21.96	22.00	25.96	20.42	17.00	20.11	
CaO	19.91	20.79	20.13	15.96	10.51	11.17	10.71	7.62	14.77	15.37	16.95	
Na_2O	0.70	0.83	0.59	2.31	1.17	1.23	1.47	0.83	1.04	2.24	0.93	
K_2O	0.04	bdl	0.04	0.14	bdl	bdl	0.09	bdl	bdl	bdl	bdl	
Total	100.04	99.99	99.62	99.69	99.45	100.10	100.62	99.47	99.72	100.25	100.03	
mg-no.	93.39	92.96	91.50	77.10	87.78	87.55	86.27	88.94	89.43	90.30	90.90	
SiO_2/Al_2O_3	76.89	77.56	27.58	5.40	13.41	13.29	12.05	18.31	16.76	11.04	16.49	
Run:	178	178	176	176	176	177	177	173	173	173	173	173
P (GPa)/T (°C)	2/975	2/975	2/1025	2/1025	2/1025	2/1025	2/1025	2/1300	2/1300	2/1300	2/1300	2/1300
SiO_2	54.06	54.49	54.95	54.95	53.40	54.83	53.53	51.66	53.18	53.65	53.77	53.43
TiO_2	0.05	0.08	0.09	0.11	0.17	0.29	0.87	1.38	0.37	0.57	0.66	0.10
Al_2O_3	3.28	2.91	1.65	1.60	4.20	3.85	6.18	7.88	7.13	7.30	8.39	6.44
Cr_2O_3	0.75	1.05	2.52	2.31	0.64	0.97	2.08	1.09	1.66	1.29	1.29	1.83
FeO^T	1.86	1.94	2.20	2.24	3.70	3.79	5.75	8.84	4.20	4.25	4.13	3.78
MnO	0.05	0.06	0.09	0.21	0.26	0.14	0.17	0.29	0.17	0.21	0.15	0.06
MgO	17.41	16.93	18.25	18.83	16.55	16.46	14.08	14.72	18.36	17.55	17.37	18.05
CaO	20.72	21.46	19.43	18.96	18.60	18.13	14.02	11.12	11.97	10.93	9.72	14.18
Na_2O	1.53	1.34	1.25	1.27	1.89	2.45	3.90	3.41	2.75	3.63	4.14	2.27
K_2O	0.19	0.27	bdl	bdl	0.04	bdl	bdl	0.07	bdl	bdl	bdl	0.04
Total	99.90	100.53	100.43	100.48	99.45	100.91	100.58	100.46	99.79	99.38	99.62	100.18
mg-no.	94.32	93.93	93.64	93.72	88.81	88.51	81.29	74.71	88.58	87.99	88.18	89.44
SiO_2/Al_2O_3	16.48	18.73	33.30	34.34	12.71	14.24	8.66	6.56	7.46	7.35	6.41	8.30

mg-number $= Mg \times 100/(Mg + Fe^T)$; bdl, below detection limit.

Table 4. *Representative electron microprobe analyses of sp1 and sp2 in lherzolite*

Run	169	169	167	170	173	176	176	176	177	177	178
	sp1	sp2	sp2	sp1	sp1	sp1	sp2	sp2	sp2	sp2	sp1
P (GPa)/T (°C)	1.5/1150	1.5/1150	1.5/1200	1.5/1250	2/1300	2/1025	2/1025	2/1025	2/1025	2/1025	2/975
TiO_2	0.07	0.11	0.11	0.59	0.32	0.10	0.15	0.07	1.81	1.21	bdl
Al_2O_3	46.42	35.42	22.56	44.05	42.63	46.83	33.68	24.29	14.68	15.89	49.45
Cr_2O_3	22.89	36.15	47.64	22.40	27.73	22.84	32.62	42.74	41.53	41.40	21.67
FeO^T	12.43	12.77	11.79	17.25	11.54	12.06	20.49	18.60	31.57	31.04	10.78
MnO	0.11	0.15	0.16	0.14	0.08	0.13	0.42	0.32	0.47	0.51	0.13
MgO	18.68	17.30	16.67	15.18	18.49	18.93	13.72	13.14	10.49	10.84	19.81
CaO	0.02	0.06	0.14	0.15	0.02	0.07	0.14	0.05	0.12	0.08	0.00
Total	100.62	101.96	99.07	99.76	100.79	100.96	101.22	99.21	100.67	100.97	101.84
Cr-no.	0.25	0.41	0.59	0.25	0.30	0.25	0.39	0.54	0.65	0.64	0.23
Mg-no.	0.75	0.72	0.75	0.63	0.75	0.76	0.59	0.60	0.48	0.50	0.78

Mg-number $=Mg/(Mg + Fe^{2+})$ where Fe^{2+} was calculated on the basis of stoichiometry and charge balance; Cr-number $= Cr/(Cr + Al)$; bdl, below detection limit.

Table 5. *Representative electron microprobe analyses of glasses in lherzolite*

Run	170	170	170
P (GPa)/T (°C)	1.5/1250	1.5/1250	1.5/1250
SiO_2	54.64	56.96	58.27
TiO_2	1.37	0.55	0.44
Al_2O_3	21.55	21.47	22.26
Cr_2O_3	bdl	0.08	0.13
FeO^T	3.61	2.90	2.58
MnO	0.11	bdl	0.03
MgO	3.58	3.10	3.49
CaO	2.72	2.04	2.05
Na_2O	4.38	4.99	5.31
K_2O	3.68	3.91	4.29
Total	95.64	96.00	98.85

bdl, below detection limit.

section. Neoformed clinopyroxene and spinel crystals are found in the (central) lherzolitic portion of the charge. In particular, cpx2 shows slight Na_2O enrichment (up to 1.53 wt%) and CaO depletion (down to 20.7 wt%) with respect to cpx1.

Nephelinite–wehrlite runs

At 1.0 GPa the nephelinite layer of anhydrous experiments is completely molten at 1250 °C; at 1200 °C olivine crystallizes, joined by clinopyroxene at 1150 °C, and by spinel and nepheline at 1050 °C. In the hydrous experiments performed at 1150 °C and 1050 °C, crystal assemblages in nephelinite are the same as the anhydrous experiments but lack nepheline; rhönite and apatite occur at lower temperature. It is evident that at different temperatures different melt composition start to interact with the wehrlitic layer and their composition are reported in Table 8 and shown in the total alkalis–silica (TAS) diagram (large symbols in Fig. 3a).

Melts are in contact with the wehrlite through a reaction area whose extent depends on experimental temperature and run duration. The influence of the experimental time is shown by the replicated anhydrous experiment at 1150 °C: in the shorter run (8 h) the reactions are limited to a *c.* 250 μm wide area whereas in the longer runs (24 h) the reaction affects all the wehrlite layer.

Run at T = *1250 °C.* The wehrlite layer is strongly infiltrated and three sub-layers can be recognized (Fig. 2): in the boundary layer (layer I), 300 μm wide closest to nephelinite melt, clinopyroxene (cpx1) dissolved completely, resulting in a mush of olivine + melt (Fig. 2a). The melt composition in this region is controlled by the contribution of cpx1 dissolution in the nephelinite; the resulting

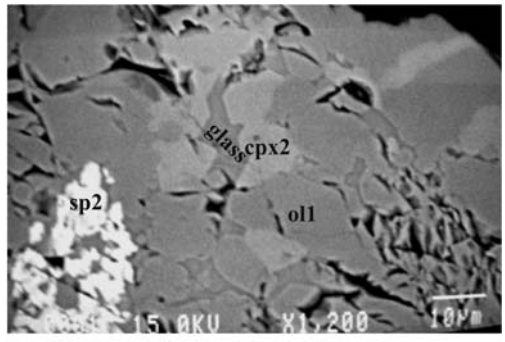

(a)

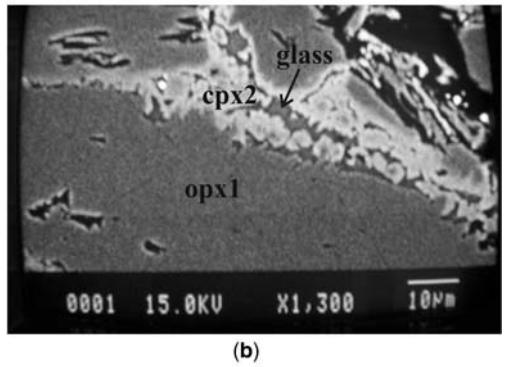

(b)

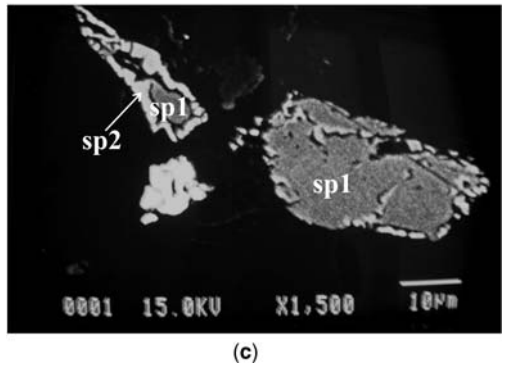

(c)

Fig. 1. Backscattered electron images of representative run products in lherzolite. (**a**) Run 170 (1250 °C and 1.5 GPa); (**b**, **c**) run 169 (1150 °C and 1.5 GPa).

melt is enriched in SiO_2 and CaO, and depleted in alkalis (mainly Na_2O), TiO_2 and P_2O_5 (Tables 6–8; Fig. 3a–d). The mg-number is close to that of nephelinite.

The olivine grains become more rounded or show embayed rims; the composition is depleted in iron (Fo 82.6) relative to primary olivine (Fo 80.8; ol1). Calculated partition coefficients ($K_{D\ Mg/Fe}$) for Mg and Fe (all Fe as FeO) between

Table 6. *Representative electron microprobe analyses of ol2 in wehrlite*

Run	141 ol1*	141 ol2†	141 ol2	141 ol1‡	140 ol2§	140 ol2	140 ol2§	153 ol2§	153 ol2¶	153 ol2§	153‖ ol2§	153‖ ol2
T (°C)	1250	1250	1250	1250	1200	1200	1200	1150	1150	1150	1150	1150
SiO_2	39.06	39.57	40.19	40.02	38.77	38.56	38.69	37.99	38.53	39.21	38.19	38.88
TiO_2	bdl	bdl	bdl	bdl	0.02	0.14	0.03	bdl	bdl	bdl	bdl	bdl
Al_2O_3	0.12	bdl	bdl	bdl	0.09	0.32	0.03	0.04	0.03	0.03	0.24	0.05
FeO	16.00	14.58	15.43	14.33	23.16	23.95	21.36	22.91	21.18	19.85	21.21	24.00
MnO	0.39	0.21	0.30	0.10	0.42	0.40	0.49	0.36	0.37	0.34	0.48	0.44
MgO	42.75	44.10	44.09	44.77	36.43	35.83	38.86	37.07	39.57	39.81	38.32	36.91
CaO	0.42	0.39	0.58	0.35	0.44	0.50	0.32	0.62	0.56	0.47	0.54	0.50
NiO	0.24	0.18	0.12	0.18	0.27	0.19	0.19	0.10	0.15	0.23	bdl	0.11
Cr_2O_3	0.17	bdl	0.20	0.12	0.04	0.02	bdl	0.09	0.14	0.02	0.12	0.07
Total	99.15	99.03	100.91	99.87	99.64	99.91	99.97	99.18	100.54	99.96	99.10	100.94
Fo	82.65	84.36	83.59	84.78	73.71	72.73	76.43	74.26	76.91	78.14	76.31	73.28

Run	154 ol2	154 ol2¶	154 ol2¶	154‖ ol2	154‖ ol2	154‖ ol2¶	154‖ ol2¶
T (°C)	1050	1050	1050	1050	1050	1050	1050
SiO_2	37.25	37.57	39.81	37.69	38.16	39.83	39.63
TiO_2	bdl	bdl	bdl	bdl	bdl	bdl	bdl
Al_2O_3	0.03	0.22	0.02	0.02	0.19	bdl	0.25
FeO	32.52	28.82	20.16	30.69	27.68	19.30	17.84
MnO	0.73	0.59	0.35	0.56	0.43	0.34	0.21
MgO	28.99	32.31	39.35	30.59	33.46	40.10	41.18
CaO	0.53	0.43	0.23	0.50	0.41	0.35	0.07
NiO	0.02	0.09	0.17	0.09	0.10	0.19	0.17
Cr_2O_3	0.10	bdl	0.20	bdl	0.08	bdl	0.22
Total	100.18	100.03	100.29	100.14	100.51	100.10	99.57
Fo	61.38	66.64	77.67	63.99	68.31	78.81	76.43

*Restitic olivine in layer.
†Restitic olivine in layer II.
‡Restitic olivine in layer III.
§Analysis at the rim of ol1 at nephelinite–wehrlite boundary layer.
¶Away from nephelinite–wehrlite boundary layer.
‖Wet experiments.
Fo, forsterite; bdl, below detection limit.

olivine and the associated melt range from 0.23 to 0.26. The highest $K_{D\ Mg/Fe}$ values approach the equilibrium values of 0.3 ± 0.03 for mafic melts (Roeder & Emslie 1970).

Layer II, about 600 μm wide, is composed of olivine, clinopyroxene and interstitial melt that may contain neocrysts of olivine and clinopyroxene (Fig. 2a and b). The melt fraction of this layer is very low relative to layer I and the glass occurs in interstitial patches rarely connected to olivine + melt layer by very thin veins. Neoformed olivines crystallized in the largest glass blebs are subequant and up to 25 μm in size whereas neoformed clinopyroxenes are anhedral and similar in size to the neoformed olivines. The primary crystals generally preserve their original shape, showing slightly rounded rims when they occur close to the small glass blebs; sometimes original olivines close to the large blebs show an overgrowth of neoformed olivine (Fig. 2b).

The compositional variation observed in the primary phases consists in the enrichment of forsterite component in olivine (from Fo *c.* 80 in ol1 to an average of Fo 84.3 in ol2) and depletion in TiO_2, Al_2O_3, FeO and Na_2O, as well as an increase in mg-number, in clinopyroxenes (Table 7). These compositional changes indicate a restitic character for these crystals (Hirose & Kawamoto 1995; Shaw *et al.* 2006).

Compositions of the interstitial glass pools, reported in Table 8, differ significantly from those of glasses at the nephelinite–wehrlite interface ('boundary layer'). Moving towards layer III, as melt pools decrease in size, the compositions change, displaying an increase in SiO_2, Al_2O_3, FeO and alkalis (Na_2O to a minor extent), and a decrease of TiO_2, CaO, P_2O_5 and mg-number (Table 8 and Fig. 3).

The secondary olivine (ol2) grown in the largest melt pools has similar composition to restitic olivine (an average of Fo 83.5) whereas secondary clinopyroxene (cpx2) is enriched in TiO_2 (1.1–2.7 wt%), Al_2O_3 (4.2–7.2 wt%), FeO (6.2–10.4 wt%) and Na_2O (1.0–1.6 wt%) (Fig. 4a–c) with respect to cpx1 (Tables 6 and 7). The mg-number of cpx2 ranges from 66 and 74 (Table 7).

Restitic olivine has $K_{D\ Mg/Fe}^{ol/liquid}$ between 0.03 and 0.19, whereas $K_{D\ Mg/Fe}^{ol/liquid}$ between ol2 and the associated melt ranges from 0.14 to 0.17, all consistently lower than equilibrium values. The lowest $K_{D\ Mg/Fe}^{ol/liquid}$ values are related to glass with the highest SiO_2 content. $K_{D\ Mg/Fe}^{cpx/liquid}$ (all Fe as FeO) of restitic clinopyroxene falls outside the equilibrium range of 0.25–0.32 (Nielsen & Drake 1979; Shaw *et al.* 1998), and varies between 0.08 and 0.12. Conversely, the $K_{D\ Mg/Fe}$ values for cpx2 and melt pairs are close to equilibrium values, ranging from 0.26 to 0.38.

In layer III, the most distal from the nephelinite–wehrlite interface (Fig. 2a), olivine and clinopyroxene have compositions similar to those of 'restitic' crystals in layer II but fractions of secondary melt are very low and are not large enough to be analysed.

Runs at $T < 1250\ ^{\circ}C$. As in the 1250 °C run, the wehrlite layer shows various degree of interaction with infiltrated melts. In all experiments the boundary layers (on average 250 μm wide) are characterized by the highest melt fraction; the reaction between liquid and wehrlite results in a decrease in clinopyroxene abundance and growth of neoformed olivine, which occurs either as discrete grains or rims on the original crystals. In the remaining wehrlite, the infiltrating melt forms small patches or a network of thin veins and interstitial glass pools spreading across the entire wehrlite layer. In the short duration (8 h) experiment at 1150 °C the melt–rock interaction area is restricted to a narrow area (about 100 μm in diameter).

Minerals

The neoformed olivine crystallized at the boundary layer is depleted in the Fo component with respect to ol1, approaching the composition of olivine crystallizing in the nephelinite area (from Fo76 for ol2 at 1200 °C to Fo61 for ol2 at 1050 °C; Table 6). Dissolution of initial clinopyroxene in this region strongly decreases from the run at 1200 °C to that at 1050 °C.

In the wehrlite, primary olivine and clinopyroxene do not show significant textural variations and olivine neocrysts may grow in the largest melt pools. The olivine neocrysts progressively approach the composition of ol1 (Table 6). Original clinopyroxene (cpx1) develops narrow (up to 50 μm) and irregular reaction rims (cpx2; Fig. 2c) enriched in TiO_2 (up to 1.25 wt% at 1200 °C; up to 5.55 wt% at 1050 °C), Al_2O_3 (up to 5.4 wt% at 1200 °C; up to 8.9 wt% at 1050 °C), FeO (up to 6.5 wt% at 1200 °C; up to 9.2 wt% at 1050 °C) and Na_2O (0.8 wt% at 1200 °C; up to 1.4 wt% at 1050 °C). These enrichments are coupled with decreasing mg-number values (Table 7 and Fig. 3a–d) (see also Shaw *et al.* 2006, and references therein). It is noteworthy that the cpx2 compositions of each experimental run are related to the composition of the reacting melt, which in turn depends on the experimental temperature (Fig. 3e). Some of the scatter observed in each compositional trend is due to the irregular extent of the melt–rock reactions (Fig. 2c).

In the hydrous experiments at 1150 °C and 1050 °C, cpx1 dissolution at the interface with the

Table 7. *Representative electron microprobe analyses of cpx2 in wehrlite*

Run	141 cpx restitic	141 cpx2*	141 cpx2*	140 cpx2†	140 cpx2‡	153 cpx2‡	153 cpx2*	153§ cpx2†	153§ cpx2†	154 cpx2‡	154 cpx2‡	154 cpx2*
T (°C)	1250	1250	1250	1200	1200	1150	1150	1150	1150	1050	1050	1050
SiO_2	54.11	47.89	50.09	50.54	49.63	46.73	50.88	48.57	51.56	45.29	47.76	50.63
TiO_2	0.28	2.71	1.45	1.25	1.08	2.84	1.55	2.47	1.24	3.92	2.30	1.12
Al_2O_3	1.46	6.17	4.79	5.44	4.91	7.72	5.03	5.54	3.38	7.90	6.61	4.87
Cr_2O_3	1.39	0.31	0.23	0.88	0.88	0.57	0.73	0.28	0.75	0.07	0.15	0.65
FeO^T	4.17	10.24	8.75	6.55	6.24	6.13	4.93	7.79	5.73	9.13	8.24	6.42
MnO	0.10	0.36	0.23	0.16	0.11	bdl	0.07	0.11	0.05	0.26	0.33	bdl
MgO	16.35	11.24	13.52	14.44	15.84	12.80	14.51	12.75	15.19	10.31	12.73	15.22
CaO	21.05	20.14	19.51	19.93	20.44	21.71	21.37	20.83	21.81	22.41	20.46	19.71
Na_2O	0.55	1.40	1.54	0.74	0.81	1.19	1.11	1.18	0.64	1.00	1.15	0.83
Total	99.46	100.46	100.11	99.93	99.95	99.69	100.18	99.53	100.36	100.29	99.73	99.45
mg-no.	87.49	66.18	73.37	79.72	81.90	78.83	83.99	74.48	82.54	66.81	73.36	80.87
SiO_2/Al_2O_3	37.06	7.76	10.46	9.29	10.11	6.05	10.12	8.77	15.25	5.73	7.23	10.40

Run	154§ cpx2‡	154§ cpx2c‡ (rim)	154§ cpx2‡	154§ cpx2‡
T (°C)	1050	1050	1050	1050
SiO_2	46.94	45.83	44.53	46.91
TiO_2	2.70	2.49	5.33	2.94
Al_2O_3	7.54	8.95	10.64	7.80
Cr_2O_3	bdl	bdl	0.42	0.08
FeO^T	9.65	8.78	7.70	9.30
MnO	0.19	0.13	0.16	0.25
MgO	10.30	10.61	9.60	10.30
CaO	21.52	21.43	20.99	20.79
Na_2O	1.04	1.11	1.29	1.32
Total	99.88	99.33	100.66	99.67
mg-no.	87.49	66.18	73.37	79.72
SiO_2/Al_2O_3	37.06	7.76	10.46	9.29

*cpx2 neocrysts in glass blebs far from SAX20–wehrlite boundary layer.
†Clinopyroxene reacted rim analysed far from SAX20–wehrlite boundary layer.
‡cpx2 at boundary layer.
§Wet experiments.
mg-number= $Mg \times 100/(Mg + Fe^T)$; bdl, below detection limit.

Table 8. *Representative electron microprobe analysis of glasses in wehrlite*

Run	141 glass*	141 glass*	141 glass*	141 glass†	141 glass†	141 glass†	141 glass†	140 nephelinite derived melt	140 glass*	140 glass†	153 nephelinite derived melt	153 glass*	153 glass†
T (°C)	1250	1250	1250	1250	1250	1250	1250	1200	1200	1200	1150	1150	1150
SiO_2	45.86	46.28	48.26	47.34	49.23	50.63	51.69	42.24	45.12	46.28	42.4	42.56	44.52
TiO_2	2.66	2.47	2.05	2.72	2.15	1.95	2.13	3.48	4.09	3.91	4.23	4.25	4.36
Al_2O_3	9.74	9.34	8.29	9.84	9.12	13.13	13.34	13.21	13.88	14.16	14.07	13.94	14.67
Cr_2O_3	0.22	0.76	0.28	0.26	0.35	0.52	0.06	0.06	0.10	bdl	bdl	0.05	bdl
FeO^T	13.64	13.47	13.14	12.37	12.13	17.28	13.38	14.35	11.84	11.84	13.85	12.74	11.41
MnO	0.23	0.29	0.26	0.23	0.31	0.35	0.25	0.34	0.31	0.25	0.25	0.28	0.37
MgO	9.11	9.42	8.13	6.00	5.10	2.01	1.20	6.58	4.82	3.15	4.56	3.63	1.74
CaO	12.24	12.45	13.64	14.52	14.49	7.61	9.47	10.22	12.82	12.81	11.73	12.66	11.45
Na_2O	4.10	4.17	4.37	4.78	5.56	4.62	5.34	5.90	5.19	5.60	5.69	5.94	7.32
K_2O	1.17	1.16	1.06	1.12	1.25	1.84	2.37	1.96	1.84	1.99	1.95	2.35	2.48
P_2O^5	1.03	0.19	0.50	0.83	0.30	0.06	0.78	1.64	na	na	1.28	1.61	1.68
mg-no.	54.35	55.49	52.45	46.37	42.83	17.16	13.79	44.98	42.06	32.17	36.99	33.69	21.38
SiO_2/Al_2O_3	4.71	4.96	5.82	4.81	5.40	3.86	3.87	3.20	3.25	3.27	3.01	3.05	3.03
Run	153‡ nephelinite derived melt	153‡ glass*	153‡ glass†	154 nephelinite derived melt	154 glass*	154 glass*	154 glass†	154 glass§	154‡ nephelinite derived melt	154‡ glass*	154‡ glass*	154‡ glass*	154‡ glass†
T (°C)	1150	1150	1150	1050	1050	1050	1050	1050	1050	1050	1050	1050	1050
SiO_2	42.60	43.93	45.76	47.85	49.76	49.4	55.03	50.2	46.74	47.59	48.26	49.9	51.25
TiO_2	3.85	3.94	3.31	2.40	1.88	2.45	1.46	1.69	2.56	2.46	2.20	2.11	1.73
Al_2O_3	13.14	15.28	16.69	19.40	21.01	20.15	22.31	21.75	19.43	19.76	19.98	21.51	23.13
Cr_2O_3	0.14	0.01	bdl	0.03	bdl	0.16	0.04	bdl	bdl	0.08	bdl	0.11	0.07
FeO^T	13.97	10.92	9.49	11.20	6.67	9.33	3.40	5.76	10.26	9.57	9.04	6.76	4.44
MnO	0.30	0.17	0.25	0.18	0.06	0.20	0.01	0.03	0.23	0.26	0.23	0.21	0.09
MgO	5.85	3.26	1.77	2.20	1.96	1.86	1.66	1.95	2.22	2.23	2.30	2.02	1.70
CaO	11.49	11.79	9.62	6.07	4.53	5.36	2.79	3.68	6.58	5.89	5.75	4.93	3.58
Na_2O	5.43	6.61	8.81	6.47	9.62	6.97	7.92	10.51	8.45	8.54	8.37	8.79	10.31
K_2O	2.00	2.04	2.05	3.10	3.67	3.44	4.45	3.82	2.94	3.07	3.12	3.66	3.70
P_2O^5	1.24	2.06	2.26	1.11	0.84	0.68	0.92	0.60	0.60	0.54	0.76	0.45	0.37
mg-no.	42.75	34.74	24.95	25.97	34.36	26.22	46.54	37.64	27.84	29.35	31.22	34.76	40.57
SiO_2/Al_2O_3	3.24	2.88	2.74	2.47	2.37	2.45	2.47	2.31	2.41	2.41	2.42	2.32	2.22

*Glass blebs at SAX20–wehrlite boundary layer.
†Glass blebs in the wehrlite layer.
‡Wet experiments.
§Glass analysed along the capsule wall.
mg-number $= Mg \times 100/(Mg + Fe^T)$; bdl, below detection limit; na, not analysed.

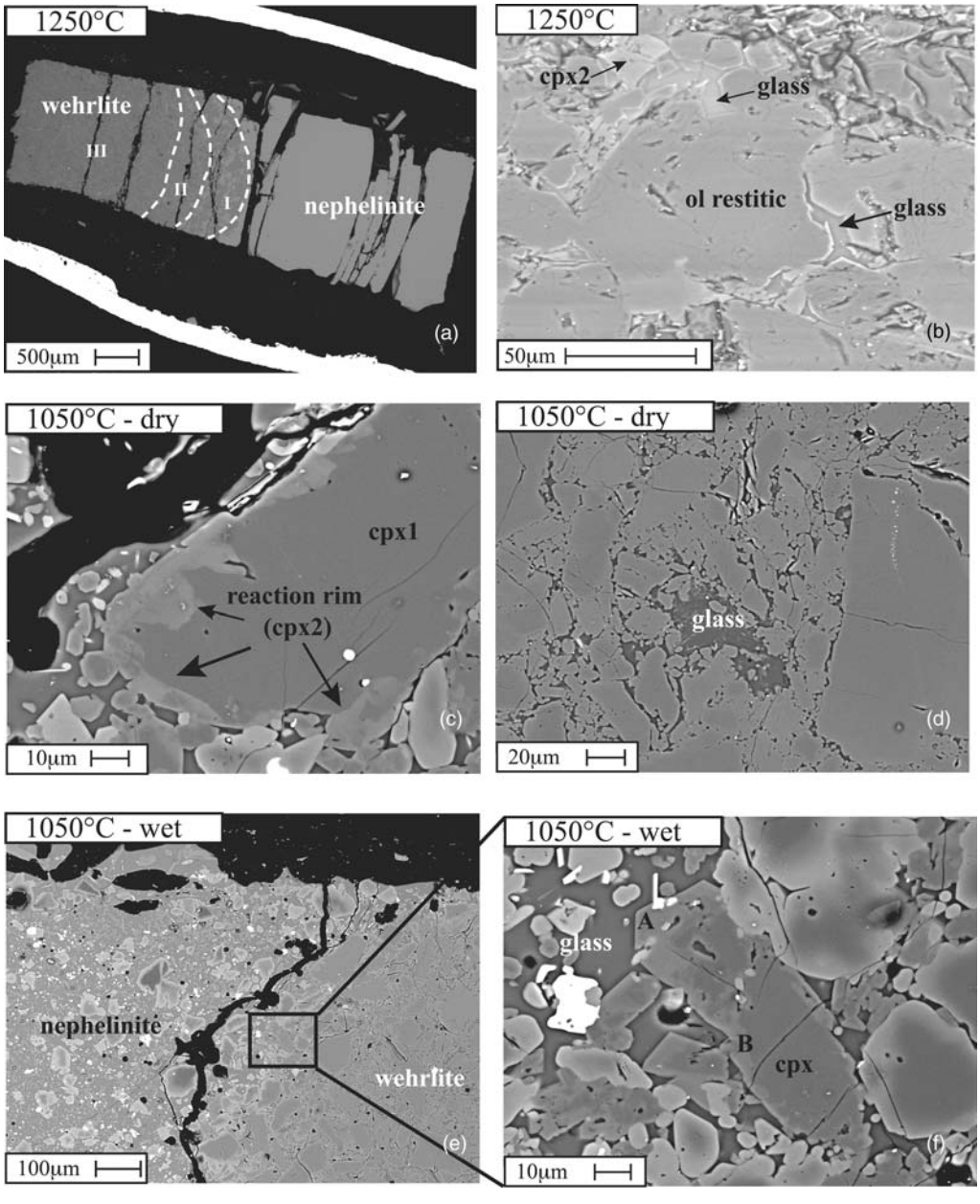

Fig. 2. Backscattered electron images of representative run products in wehrlite. (**a**, **b**) Run 141 (1250 °C), (**c**, **d**) run 154 (1050 °C); (**e**, **f**) run 154* (1050 °C, wet run). I, II and III refer to different reaction areas observed in 1250 °C run. cpx2, clinopyroxenes produced by melt–rock reaction; ol restitic, olivine that underwent partial melting (1250 °C). In (f) A refers to the growth rim on primary clinopyroxene; B refers to the reaction rim of the same crystal.

melt is reduced with respect to the anhydrous counterparts. A small amount of cpx1 dissolved completely (at 1150 °C) or partially (at 1050 °C) in an area about 200 μm wide (Fig. 2e and f). The neoformed phases found both at the interface and inside the wehrlite layer show the same kind of compositional modifications and textural features as recognized in the anhydrous experiments (Fig. 4a–c). In the 1050 °C run a Ti-rich spinel also crystallizes at the boundary layer (Fig. 2f).

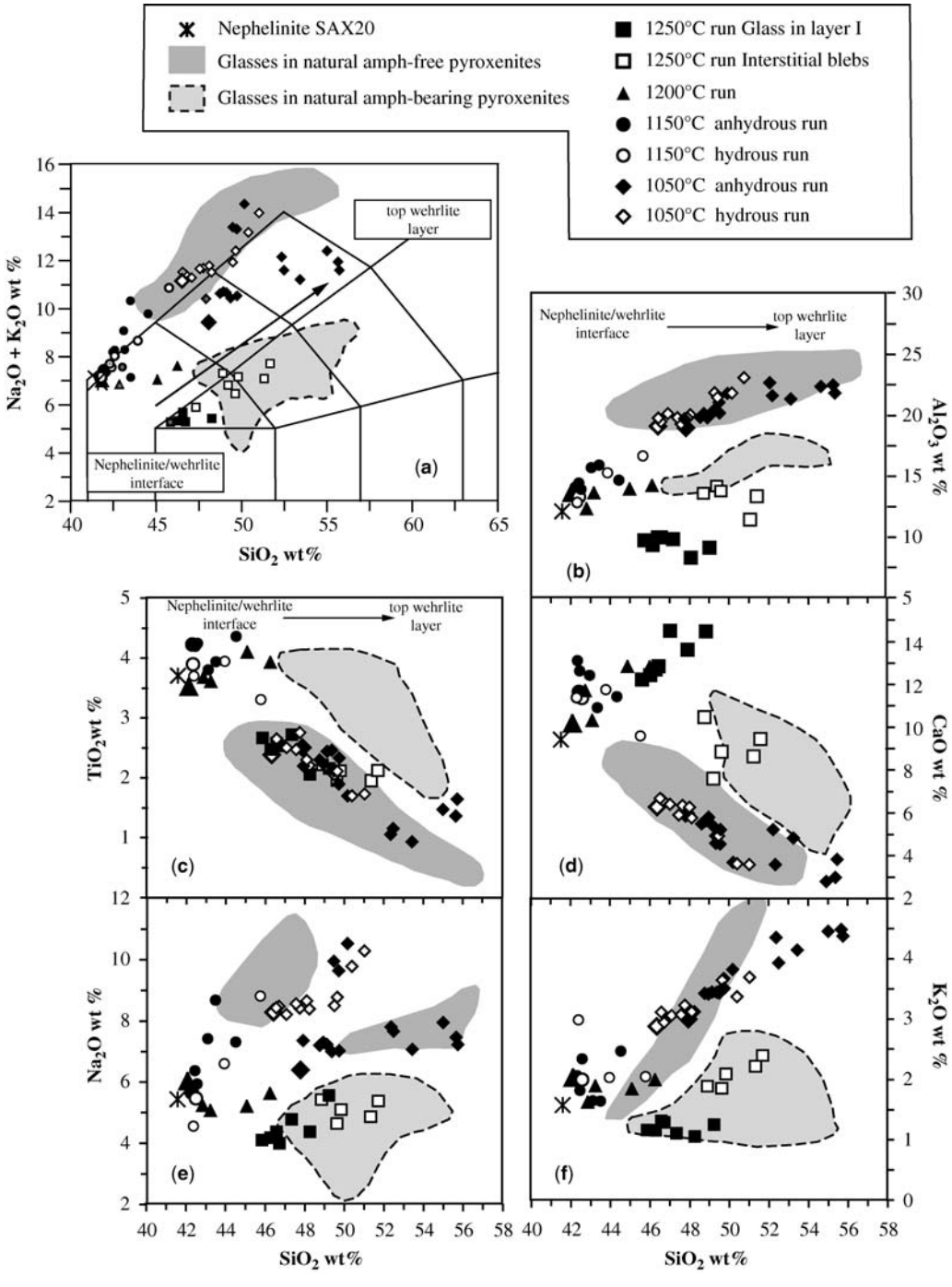

Fig. 3. (**a**) Experimental glasses from nephelinite–wehrlite runs plotted in the TAS classification diagram (Le Bas *et al.* 1986); (**b**–**f**) compositional variation diagrams for experimental glasses. The arrows indicate compositional variations resulting from the continuous interaction of infiltrating melts with the wehrlite. The large symbols represent the nephelinite-derived melts; asterisk indicates the melt composition at the boundary layer that starts infiltration. Also shown are fields for interstitial glasses occurring in natural wehrlites (Perinelli & Armienti unpublished).

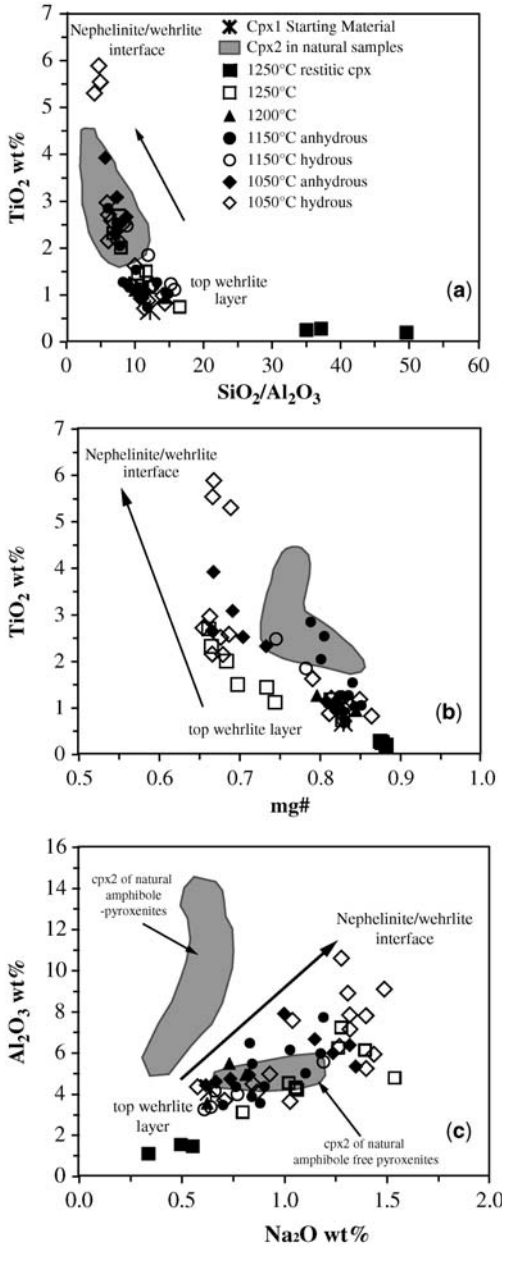

Fig. 4. (**a**) TiO_2 v. SiO_2/Al_2O_3, (**b**) TiO_2 v. mg-number, and (**c**) Al_2O_3 v. Na_2O, for synthesizing clinopyroxenes in nephelinite–wehrlite experiments. Also shown is secondary clinopyroxene related to metasomatism of natural wehrlites (grey area; Perinelli & Armienti 2005). The long arrows indicate compositional variations induced by metasomatism on original clinopyroxene as a function of distance from the nephelinite–wehrlite boundary layer.

Glasses

A network of melt veins and/or interstitial glass pools is observed in all the experiments. This is connected to the nephelinite. Melt compositions of the analysable glass are reported in Table 8.

In the 1200 °C and 1150 °C experiments, including the longest duration run at 1150 °C, most of the interstitial pools were too small to be analysed. Glasses analysed at the boundary layer show weak chemical modifications with respect to nephelinite, except for alkalis (mainly Na_2O), which were enriched in the experiments at 1150 °C. The same enrichment was not observed in glasses from the 1200 °C run, the chemistry of which records instead the higher contribution of clinopyroxene dissolution (Table 8; Fig. 3a–f).

In the hydrous and anhydrous experimental runs performed at 1050 °C, the melts occurring at the boundary layer and invading wehrlite have the most differentiated compositions (Fig. 3a), being derived by high degrees of nephelinite crystallization at this temperature; further inside the rock, these melts show an increase in SiO_2 (to 55%) and K_2O (to 4.5%) and a depletion in CaO, P_2O_5 (not shown) and TiO_2 (although these last two elements show an increase at the top of wehrlite; Fig. 3c). In these runs, Na_2O content in the melt patches is influenced by the presence of water, which prevented the nepheline crystallization in the hydrous nephelinite-derived melt; as a consequence, Na_2O concentrations in wet experiments are higher than in anhydrous ones, reaching 10 wt% in the distal interstitial patches. Similar Na content is attained in the water-free runs only in the melt portions that occur along the wall of the graphite capsule (Fig. 3e).

It is noteworthy that the mg-number values shown a good covariance with SiO_2 (not shown).

In terms of mineral–melt Mg and Fe exchange equilibrium we found that olivine $K_D^{ol/liquid}{}_{Mg/Fe}$ (0.27–0.33) and clinopyroxene $K_D^{cpx/liquid}{}_{Mg/Fe}$ (0.2–0.28) in the boundary layer approach equilibrium values for the highest temperature experiment (1200 °C) or the longest duration runs (1050 °C, 48 h). In the wehrlite layer the $K_D^{ol/liquid}{}_{Mg/Fe}$ values are generally lower (0.15–0.18) than those calculated for the boundary layer, although $K_D^{cpx/liquid}{}_{Mg/Fe}$ shows a very wide range (0.12–0.35), with most values falling in the range 0.24–0.30, indicating equilibrium between most of the clinopyroxenes and associated melts. The low K_D values for olivine may be due to the high SiO_2 content of the glass occurring in this area (Draper & Green 1997; Shaw *et al.* 1999).

$K_D^{phases/liquid}{}_{Mg/Fe}$ values computed for 1150 °C experiments are constantly low (<0.19 and <0.18

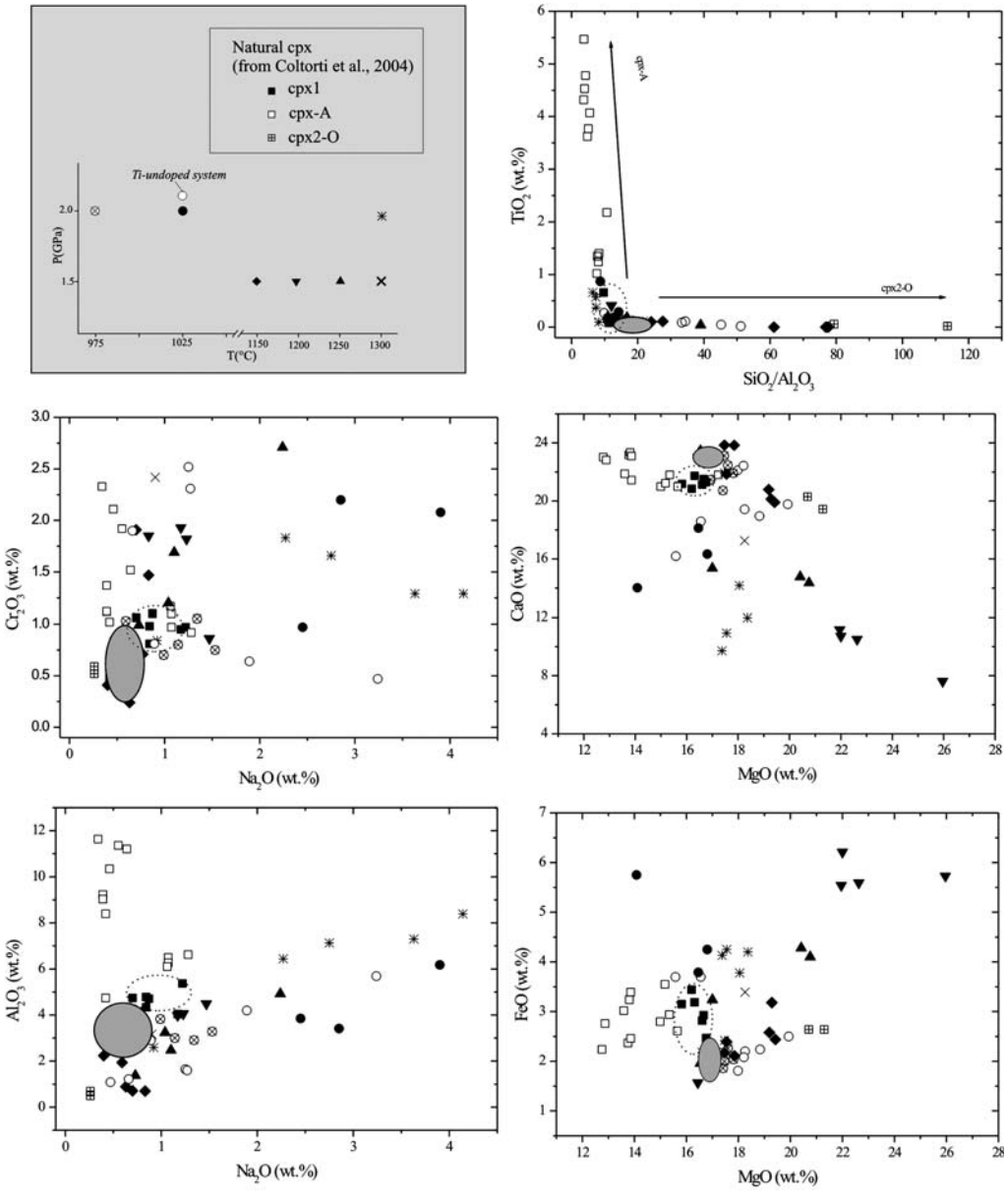

Fig. 5. Composition of experimental (this paper) and natural clinopyroxenes (from Coltorti *et al.* 2004). The shaded area and dotted line indicate the compositional field of cpx1 of lherzolite 154L (this paper) and cpx1 from Coltorti *et al.* (2004), respectively. The arrows in the upper right diagram indicate out compositional variations induced by metasomatism on cpx1, as reported by Coltorti *et al.* (2004).

for olivine and clinopyroxene, respectively). These low K_D values are not linked to the occurrence of high SiO_2 melts and may be related to the run duration being too short to attain equilibrium.

Discussion

The ubiquitous occurrence of neoformed clinopyroxene and spinel in the lherzolite and clinopyroxene and olivine in the wehrlite indicates that both

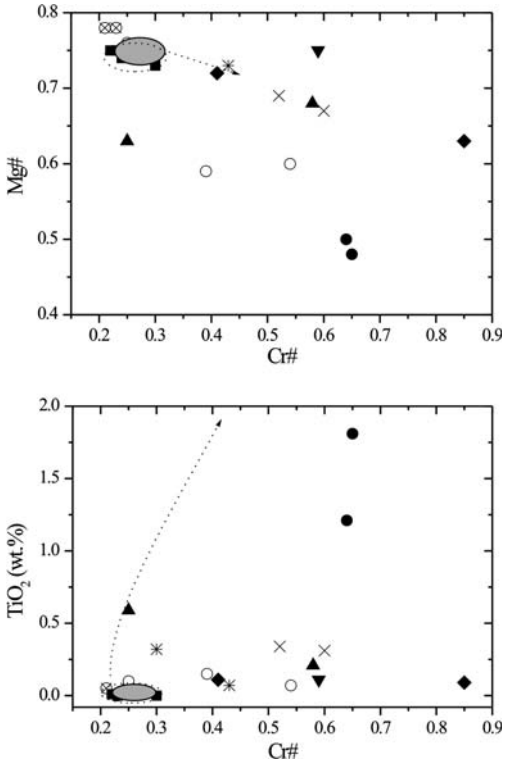

Fig. 6. (**a**) Cr-number v. Mg-number and (**b**) Cr-number v. TiO_2, in experimental spinel. Legend as in Figure 5. The dotted arrows indicate compositional variations induced by metasomatism on original spinels from mantle xenoliths (Coltorti *et al.* 2004).

underwent a chemical modification at the experimental conditions. The modifications observed in lherzolite and wehrlite will be discussed below.

Nephelinite–lherzolite reaction

The distribution and the paucity of the glass do not allow a reaction front to be clearly identified in the lherzolitic portion of the charges. This can be ascribed to fast kinetics of the melt infiltration process, which reaches an early completion even in the shortest run, as a consequence of the low viscosity of nephelinite-derived melts. This affects the spatial distribution and chemical composition of the neoformed phases, which do not show regular compositional variations from the lherzolite–nephelinite interface to the internal parts of the peridotite.

Neoformed minerals (cpx2, sp2) could form either by a partial melting process of lherzolite or by metasomatic reactions. However, the chemical variations recorded in cpx2 are not compatible with partial melting (e.g. their Na_2O and Al_2O_3 contents) and, although the Cr-number increase from sp1 to sp2 could be due also to partial melting (e.g. Matsukage & Kubo 2003), the fact that Cr-number variations are unrelated to temperature of the experiments rules out this hypothesis. Moreover, an increase of Cr-number in spinels is reported to occur as a result of metasomatic reactions in lherzolite (e.g. Francis 1976; Neal 1988; Sen & Dunn 1994). In addition, the fact that TiO_2 content in sp2 increases if a Ti-doped nephelinite is used clearly indicates that neoformed phases result from interaction with the alkaline melt. Textures observed in lherzolite for neoformed phases point to rock–melt interaction. In particular, the occurrence of cpx2 together with glass in association with orthopyroxene (and olivine) is reported to be a consequence of orthopyroxene interaction with silica-undersaturated melts (Shaw *et al.* 1998; Shaw 1999). Moreover, sp2 coronas observed around original spinel crystals closely resemble those reported by Shaw *et al.* (2006) in mantle peridotite xenoliths that underwent interaction with silica-undersaturated melts.

The main compositional features of cpx2 and sp2 can be compared with those of natural phases thought to be a consequence of reaction with metasomatizing melts. In Figures 5 and 6 the compositions of neoformed clinopyroxene and spinel in the lherzolitic portion of the capsule are given, together with that of original phases in lherzolite 154L. Furthermore, clinopyroxenes from unmetasomatized xenoliths and clinopyroxene associated with amphibole (cpx-A) and secondary clinopyroxenes (i.e. in the reaction rim of orthopyroxene, cpx2-O) studied by Coltorti *et al.* (2004) are also reported for comparison.

The higher Na_2O contents and the concomitant increase in Al_2O_3 and Cr_2O_3 (Fig. 5) of cpx2 synthesized at 2 GPa is a result of the entrance of trivalent cations (Al, Cr, Fe) at the M1 site as a result of the decrease in cell volume at increasing pressure. Such a high Na_2O increase is not observed in crystals formed at 1.5 GPa or in natural lherzolitic samples in which cpx-A coexists with pargasitic amphibole (containing *c.* 3 wt% Na_2O).

The Cr_2O_3 contents in cpx2 are comparable with those of cpx-A, whereas cpx2-O shows contents similar to some cpx2 formed at 1150 °C. MgO enrichment (Fig. 5) associated with CaO depletion occurs in the experimentally produced clinopyroxenes but not in cpx-A.

The SiO_2/Al_2O_3 v. TiO_2 diagram has been used by Coltorti *et al.* (2004) to show the chemical variations of both cpx-A and cpx2-O. In particular, according to those workers, TiO_2 in cpx-A approaches 6 wt% (Fig. 5) Some cpx2 crystals (formed at 2 GPa) show TiO_2 enrichments to

1 wt%, whereas SiO_2/Al_2O_3 ratios of cpx2 formed at low temperature (especially at 1150 °C) approach those of cpx2-O.

In summary, cpx2 chemistry does not match that of natural samples, although SiO_2/Al_2O_3 ratios detected in cpx2-O (from natural metasomatized lherzolites) is approached by some cpx2 synthesized at low temperature.

For spinel, Cr-number and Mg-number appear to be inversely correlated and TiO_2 content approaches 2.0 wt% in runs performed using the Ti-doped starting material (Fig. 6). No worthwhile comparison can be drawn between these findings and the data reported by Coltorti *et al.* (2004) because of the paucity of the analytical data for spinels reported by those workers. However, it can be noted that a general Cr-number and TiO_2 increase and a slight Mg-number decrease were also observed in natural sp2 (Fig. 6).

Finally, analyses of glass obtained at 1250 °C approach the composition of some Si-rich glasses found in xenoliths where interaction involving orthopyroxene occurs (Shaw *et al.* 1998; Shaw 1999). In the discrimination diagram $CaO + Na_2O$ v. $TiO_2 + K_2O$ proposed by Coltorti *et al.* (2000) to identify the nature of the metasomatic agents, these glasses plot in the field pertaining to metasomatism caused by Na-alkaline silicate melt.

Nephelinite–wehrlite reaction

The effects of metasomatic reactions recognized in the wehrlite–nephelinite experimental runs were compared with those observed in metasomatized wehrlites and pyroxenites from Browning Pass, Baker Rocks and Mt. Overlord (NVL), Antarctica. These metasomatized rocks, both amphibole-free and amphibole-bearing, are interpreted to be the result of successive infiltration of rising alkaline melt(s) into pyroxenite bodies formed by a fractionation process at different conditions of pressure and temperature (Perinelli & Armienti 2005).

The compositional features recorded by clinopyroxene in our experiments reveal the most representative effects of the reactions with the infiltrating melt. The differences between original and secondary clinopyroxenes, and the comparison of the latter with the cpx2 in natural samples, are evaluated on the basis of their TiO_2, Na_2O, SiO_2 and Al_2O_3 contents and mg-number, which are the most distinguishable chemical parameters. Experimental neoformed clinopyroxenes define a trend of decreasing SiO_2/Al_2O_3 with increasing TiO_2, from the less to the more reacted crystals (Fig. 4a); these last overlap the trend defined by neoclinopyroxenes in natural metasomatized pyroxenites (Fig. 4a). The enrichment of TiO_2 in experimental cpx2 is also associated to the increase of FeO content, which, in terms of mg-number, shows a trend similar to that of natural cpx2 although the latter displays a more limited mg-number variation (Fig. 4b). It is noteworthy that in the area of the experimental boundary layer, the distribution of TiO_2 and FeO enrichments along the reaction rims surrounding primary clinopyroxenes may be not correlated. For instance, the clinopyroxene shown in Figure 2f has similar mg-number (point A mg-number = 68.9 and point B mg-number = 68.3) along the entire reaction rim, and this results in equilibrium with the adjacent melt in term of $K_D^{cpx/liquid}{}_{Mg/Fe}$ (0.24 and 0.25, respectively), but the TiO_2 content is very different (point A TiO_2 5.33 wt% and point B TiO_2 2.49 wt%). This may be due to the different diffusive rates of these elements and to the amount of glass adjoining the crystal: the higher diffusive velocity of Fe (and Mg) with respect to Ti allows crystal–liquid equilibrium to be reached also when the amount of adjacent glass is low; when the clinopyroxene borders large melt pools and the crystal can grow, the new composition approaches that of clinopyroxenes crystallized in the nephelinite area that show very high TiO_2 content (up to 6 wt%).

The mutual variation of Na_2O and Al_2O_3 of experimental cpx2 follows a smooth positive trend that includes also some natural secondary clinopyroxenes found in the metasomatized amphibole-free pyroxenites. Most of the natural cpx2, instead, defines a steeper trend with a slight (or no) Na_2O increase (Fig. 4c). These natural cpx2 grains almost all occur in amphibole-bearing samples, suggesting that the crystallization of amphibole may affect the Na_2O behaviour in clinopyroxene. Sen & Dunn (1994) in their experimental work on melt–lherzolite interaction observed a similar relationship between amphibole crystallization and Na_2O content of associated clinopyroxene.

In this framework, the compositional modifications recorded by clinopyroxene in our reaction experiment on wehrlite are like those observed in both experimental and natural mantle rock–melt systems where the reactions involves high melt/rock volume ratio (e.g. Sen & Dunn 1994; Shaw *et al.* 1998, 2006; Shaw 1999; Coltorti *et al.* 2004; Perinelli *et al.* 2006; see the section 'Nephelinite–lherzolite reaction' of the present paper). The occurrence of amphibole, therefore, seems to be the sole parameter affecting the compositions of secondary pyroxenes in the variously metasomatized mantle rocks.

Glasses

All the glasses represent melts generated from the nephelinite. The temperature-dependent path of

nephelinite-derived melts is illustrated in the basalt tetrahedron CaTs–Di–Ol–Q pertaining to the CMAS system (Fig. 7). Nephelinite-derived compositions lie on an olivine control line down to 1150 °C; at lower temperatures clinopyroxene crystallization drives the metasomatizing melts towards a phono-tephritic composition. At the various temperatures, these are the melts that are provided to the boundary layer and start infiltration (Fig. 7).

The processes that affect the nephelinite-derived melts at the boundary layer are themselves evident in the pseudo-ternary projection from the quartz (Q) component of the basalt tetrahedron CaTs–Di–Ol–Q of Figure 7. Boundary-layer melts from

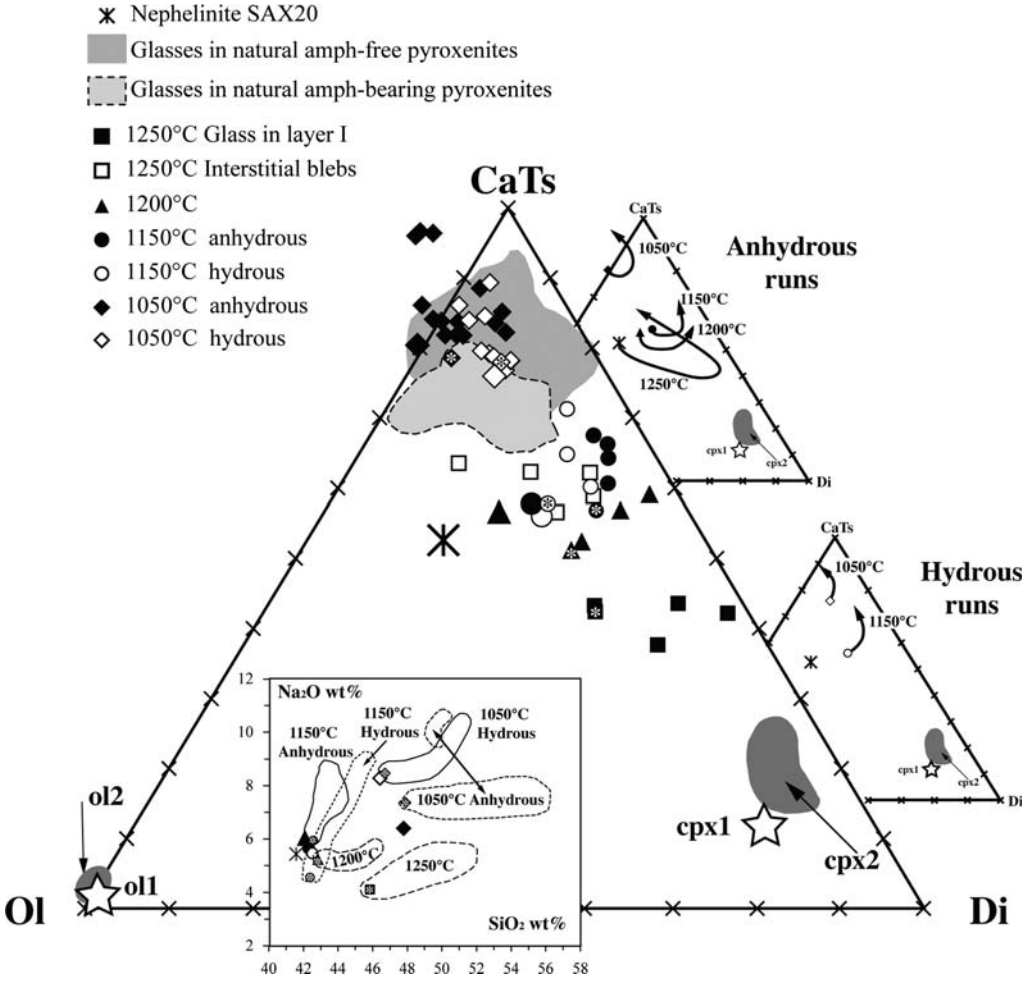

Fig. 7. Synthetic glasses plotted on the pseudo-ternary projection from quartz (Q) in the basalt tetrahedron CaTs–Di–Ol–Q pertaining to the CMAS system (O'Hara 1968), where $C = (CaO - 3.33P_2O_5 + 2Na_2O + 2K_2O) \times 56.08$, $M = (FeO + MnO + NiO + MgO - TiO_2) \times 40.31$, $A = Al_2O_3 + Cr_2O_3 + Fe_2O_3 + Na_2O + K_2O + TiO_2) \times 101.96$ and $S = (SiO_2 - 2Na_2O - 2K_2O) \times 60.09$ (all oxides in molar proportion). Symbols as in Figure 3; ol1, cpx1 and cpx2 refer to primary olivine, primary clinopyroxene and secondary clinopyroxene, respectively. In the two smaller pseudo-ternary projections the trends of liquid evolution from the nephelinite-derived melts to interstitial melts are shown for both anhydrous and hydrous experiments at the various temperatures used. The effect of alkali diffusion on the liquid compositions is shown in the inset SiO_2 v. Na_2O diagram. From this diagram it is evident that the glasses at the boundary layer of anhydrous experiments are affected by clinopyroxene dissolution mainly in the runs at the highest temperature. In the hydrous runs the clinopyroxene dissolution had negligible effect. In all experiments, the composition of melts formed in wehrlite is controlled by crystallization of new olivines and clinopyroxenes as well as by the alkali diffusion process.

higher-temperature anhydrous experiments (1250 °C–1150 °C) are influenced to a different extent by the effect of the preferential dissolution of primary clinopyroxene, which implies an increase in the abundance of cpx-derived oxides, SiO_2 and CaO (see Fig. 3). Melts from the 1150 °C hydrous run reveal, with respect to its anhydrous analogue, a negligible contribution of cpx1 dissolution and a significant crystallization of both secondary olivine and clinopyroxene. Similarly, boundary layer melts of lower-temperature runs (1050 °C), when anhydrous, show a very low assimilation of primary clinopyroxene; when hydrous, they show essentially the crystallization of neoformed olivine + clinopyroxene. These 1050 °C glasses, both hydrous and anhydrous, display a rise in alkalis and a decrease in calcium contents (Fig. 3).

The control of assimilation–crystallization processes on the composition of boundary layer melts in both hydrous and anhydrous runs is shown in more detail in the small projections of Figure 7. They show that cpx1 dissolution has a significant role in anhydrous experiments, whereas in hydrous runs, the compositional effect on the glasses of cpx1 assimilation may be hidden by the contemporaneous crystallization of neo-crystals of the same phase. Moreover, all boundary layer melts are affected by olivine crystallization. A cursory inventory of olivine and clinopyroxene amounts involved in the formation of boundary layer melts may be performed using Figure 7 and applying the lever rule. For anhydrous melts, at 1250 °C, up to 15% of olivine crystallization is necessary together with consistent (up to 40%) clinopyroxene assimilation. At lower temperatures, much lower amounts of olivine crystallization (0–5%) and clinopyroxene assimilation (10%) are required. For hydrous melts olivine and clinopyroxene crystallization always occur. It should be noted that the amount of glass is very low, and the above percentages do not imply a large amount of melting of the original paragenesis. Boundary layer melts thus appear to be controlled by clinopyroxene dissolution and/or crystallization in a way that can be recognized as a reaction front (Lundstrom 2003; Morgan & Liang 2003).

When boundary layer melts migrate through the wehrlite, they change in composition as a result of both the nucleation of new phases and reaction with pre-existing clinopyroxene and olivine. As a consequence, they progressively become enriched in SiO_2, Al_2O_3 and alkalis and depleted in TiO_2 and P_2O_5 (Fig. 3). However, the observed trends in Harker diagrams (Fig. 3 and inset in Fig. 7) seem to indicate that a diffusive flux of Na_2O and K_2O also occurrs from the nephelinite–wehrlite boundary layer into wehrlite; the interstitial pools are thus enriched in the faster diffusing elements (Na_2O and K_2O) compared with the slower diffusing TiO_2 and P_2O_5, according to a process well documented in other experimental studies ('uphill diffusion' of Shaw *et al.* 1998; see also Lundstrom 2003; Morgan & Liang 2003, and references therein). The competing behaviour between the differently diffusing TiO_2 and Na_2O is evident if we consider that the continuing clinopyroxene–melt interaction in wehrlite should reduce sodium and titanium content in the melt as a result of their absorption by clinopyroxene; instead, TiO_2 displays the expected trend whereas Na_2O increases (Fig. 3).

The continuing clinopyroxene–melt interaction in fact should change both Na_2O and TiO_2 in the same way and the decoupling of these two elements shown in Figure 3 could be explained by their different diffusivity. Moreover, the differences in the Na_2O–SiO_2 enrichment trends, shown by wet and dry experiments at 1050 °C, underline the strong effect of water on the alkali diffusivity (Freda & Scarlato 2001, and references therein).

Finally, the highest Na content attained in the water-free runs found in the melt portions along the wall of the graphite capsule may be explained by a melt advection process (Lundstrom 2003).

Although chemical transport by diffusion may have some effect on glass compositions, the different behaviour of the elements in experimental melts mainly depends on the melt/rock ratio (Navon & Stolper 1987; Bodinier *et al.* 1990; Bedini *et al.* 1997; Vernières *et al.* 1997; Ionov *et al.* 2002). For high melt/rock ratios, the compositional modification of the reactant liquid is prevented or limited to a thin layer at the melt–rock boundary (nephelinite–wehrlite interface). Low melt/rock ratios cause progressive compositional changes of percolating melt as a result of its continuous interaction with the rock assemblage. Therefore, the compositional variations of infiltrating melts and reacted phases are a function of the distance from the melt source (i.e. from the nephelinite layer) and depend on the rate of melt infiltration in addition to the reaction processes.

The compositions of experimental glasses when compared with those of natural samples reveal some significant similarities: in particular, the alkali-rich melt compositions from hydrous and anhydrous runs at 1050 °C mimic the alkali-rich glasses found in natural metasomatized amphibole-free pyroxenites (Fig. 3b–e). This suggests that in evolved T–X systems such as those experimentally reproduced at the lowest temperature, the compositions of melts probably were not suitable to form amphibole. Moreover, water content could have hindered amphibole nucleation; in fact, despite water addition in the 1050 °C run, the metasomatized assemblage contains only some spinel, a

phase that precedes amphibole nucleation in systems with low water activity (King *et al.* 2000).

Melts from runs at 1200 °C and interstitial melts at 1250 °C approach natural low-alkali melt compositions (Fig. 3a) associated with amphibole-bearing pyroxenites, although amphibole is absent in these experiments.

Lack of amphibole among experimental products

Amphibole is a phase that directly reveals metasomatism of mantle rocks and occurs in many mantle xenoliths from NVL. In our experiments, amphibole was not detected, in lherzolite or wehrlite. This was expected in high-T experiments ($T > 1100$ °C); in lower-T runs amphibole formation could have been hampered by some parameters controlling its P–T stability field in mantle rocks, such as bulk-rock composition, particularly alkali and Ti contents in lherzolite, and water content (e.g. Wallace & Green 1991; Niida & Green 1999). However, considering for comparison the Sen & Dunn (1994) reaction experiments, it can be observed that, although they used an amphibolite-derived melt as metasomatizing agent, amphibole nucleated as small (1–10 μm) grains, only at 975 °C (and not at 1025 °C) at the same pressure as our experiments (2.0 GPa).

A further parameter that may have hindered the amphibole crystallization is the melt/rock ratios in the experimental charges, which, as pointed out by Rapp *et al.* (1999), can affect the nature of chemical reactions and thus the mineralogy of the resulting assemblages.

Finally, although amphibole is outside its stability field at $T > 1100$ °C, we noted that in the wehrlite–nephelinite system the composition of melts from high-temperature runs approaches natural melt compositions associated with amphibole-bearing pyroxenites. This leads us to consider that the lack of amphibole in the runs might be due to the experimental configuration; this imposes a constant temperature on the system, a condition that does not reproduce exactly the condition of the natural environment, where a hot metasomatizing melt infiltrates a colder matrix. Therefore, high-T experimental melts could represent suitable precursors of melts able to form amphibole, but to crystallize this phase it should infiltrate a matrix at lower temperature, which is excluded by the configuration of the experiments.

Relying upon this evidence, it is possible to consider that in the mantle, where a nephelinitic magma such as SAX20 at 1200 °C passes through a relatively cool wehrlite (850-1050 °C; Perinelli & Armienti 2005; Perinelli *et al.* 2006), at the magma–wall-rock contact, the wehrlite undergoes a transient heating that induces clinopyroxene dissolution. The resultant melts, enriched in clinopyroxene components, may percolate into cooler wall rock while reacting with the wehrlitic mineral assemblage. Moreover, during their migration, melts crystallize secondary clinopyroxene and they progressively become enriched in water to achieve amphibole saturation. Similar processes, which can be accounted for in terms of 'wall-rock' metasomatism and 'diffuse' metasomatism (Xu & Bodinier 2004, and references therein), probably lead to the amphibole crystallization also in lherzolitic rocks, although our experiments with lherzolite paragenesis did not provide any indication of these processes.

Our experiments, however, do not rule out the possibility that natural glasses associated with amphibole may originate by interaction with a metasomatic agent different from SAX20 nephelinite (i.e. a low-alkali and high-TiO_2 hydrous liquid).

Concluding remarks

Although our experiments on nephelinite–lherzolite–wehrlite assemblages did not produce amphibole, considerable chemical modifications are observed in both lherzolitic and wehrlitic wehrlite assemblages portions of the charges. Moreover, the runs on nephelinite wehrlite assemblages show that compositional variations and their extent depend on melt/rock ratio and are a function of the distance from the melt source (i.e. from the nephelinite layer).

Clinopyroxene shows compositional variations in both lithotypes: it changes from diopside to high-Mg–Cr–(Na) augites and omphacites in lherzolite and to low-Mg and high-Ti–Al–Fe–Na augites in the wehrlite. Its chemical variations partially fit the modifications of clinopyroxenes found in xenoliths and thought to be a result of reactions between a metasomatizing melt such as SAX20 and a lherzolite (wehrlite). In particular, we were able to reproduce experimentally at low temperatures, the high SiO_2/Al_2O_3 ratios of secondary clinopyroxenes found as reaction rims of orthopyroxenes in lherzolite, whereas even the use of Ti-doped nephelinite did not cause the Ti increase observed in clinopyroxene of natural lherzolite. On the other hand, the Ti, Al and Na increase in natural clinopyroxenes of amphibole-free pyroxenites is fairly well matched by crystals formed in wehrlite.

Furthermore, spinel (in lherzolite) and olivine (in wehrlite) were compositionally modified by metasomatic melts: Cr-number increases and Mg-number decreases in spinel, and forsterite decreases in olivine.

Nephelinite–lherzolite experiments produced scarce interstitial glass; the only analysable patches, from the 1.5 GPa-1250 °C experiment,

have compositions that approach some melts related to orthopyroxene–melt reaction found in natural xenoliths. In contrast, experiments on the nephelinite–wehrlite system provided a variety of melts that fit to some extent the natural glasses. In particular, the runs at $T < 1150\ ^{\circ}C$ produced melts that mimic the trends shown by high-alkali and low-TiO_2 glasses found in the amphibole-free natural pyroxenites. Boundary layer glasses of high-temperature ($T > 1150\ ^{\circ}C$) runs could be the precursor of glasses associated with amphibole-bearing pyroxenites. They are significantly affected by primary clinopyroxene dissolution and simultaneous crystallization of the neoformed phases. The lack of amphibole nucleation in the experiments was probably due to the fact that the fixed temperature imposed by the experimental setting does not allow achievement of a stability field for amphibole, which can form in nature in an evolving T–X regime where a hot metasomatizing melt infiltrates a colder matrix.

This mechanism can be identified with a moving reaction front that, although implying a relatively low amount of melt, may induce widespread metasomatic effects in a wide mantle region. The variable metasomatic style recognized in NVL can be accounted for in terms of a process like this, where the infiltration of rising basaltic melts, which are also responsible for the formation of pyroxenitic lenses and dykes of variable thickness, modifies the chemical and mineralogical mantle composition, as well as its thermal regime (Armienti & Perinelli, unpublished). Such or variably metasomatized mantle source is probably responsible for the Cenozoic magmatism, although the role played by amphibole (and clinopyroxene) in the magma generation is still a matter of considerable debate.

We are grateful to C. Shaw and M. Toplis for their very constructive reviews. The authors thank M. Coltorti for helpful discussions and encouragement, F. Olmi, C. Petrone (CNR-IGG) and M. Serracino (CNR-IGAG) for help during EPM analyses, and F. Colarieti and M. Tamponi for the assistance in SEM analysis.

References

BALLHAUS, C. G., BERRY, R. F. & GREEN, D. H. 1990. Oxygen fugacity controls in the Earth's upper mantle. *Nature*, **348**, 437–440.

BEDINI, R. M., BODINIER, J.-L., DAUTRIA, J.-M. & MORTEN, L. 1997. Evolution of LILE-enriched small melt fractions in the lithospheric mantle: a case study from the East African Rift. *Earth and Planetary Science Letters*, **153**, 67–83.

BENCE, A. E. & ALBEE, A. L. 1968. Empirical correction factors for the electron microanalysis of silicates and oxides. *Journal of Geology*, **76**, 382–402.

BODINIER, J.-L., VASSEUR, G., VERNIÈRES, J., DUPUY, C. & FABRIÈS, J. 1990. Mechanisms of mantle metasomatism: geochemical evidence from the Lhèrz orogenic peridotite. *Journal of Petrology*, **31**, 597–628.

BOHLEN, S. R. B., ESSENE, E. J. & BOETTCHER, A. L. 1980. Reinvestigation and application of olivine–quartz–orthopyroxene barometry. *Earth and Planetary Science Letters*, **47**, 1–10.

COLTORTI, M., BECCALUVA, L., BONADIMAN, C., SALVINI, L. & SIENA, F. 2000. Glasses in mantle xenoliths as geochemical indicators of metasomatic agents. *Earth and Planetary Science Letters*, **183**, 303–320.

COLTORTI, M., BECCALUVA, L., BONADIMAN, C., FACCINI, B., NTAFLOS, T. & SIENA, F. 2004. Amphibole genesis via metasomatic reaction with clinopyroxene in mantle xenoliths from Victoria Land, Antarctica. *Lithos*, **75**, 115–139.

COLTORTI, M., BONADIMAN, C., FACCINI, B., MELCHIORRE, M., NTAFLOS, T & SIENA, F. 2006. Mantle xenoliths from Northern Land, Antarctica: evidence for heterogeneous lithospheric mantle. *In*: *16th Goldschmidt Conference, 27 August–1 September 2006, Melbourne, Australia, Abstracts*, A108.

DRAPER, D. S. & GREEN, T. H. 1997. P–T phase relation of silicic, alkaline, aluminous mantle-xenolith glasses under anhydrous and C–O–H fluid- saturated conditions. *Journal of Petrology*, **38**, 1187–1224.

DUNCUMB, P. & REED, S. J. B. 1968. The calculation of stopping power and backscatter effects in electron probe microanalysis. *In*: HEINRICH, K. F. J. (ed.) *Quantitative Electron Probe Microanalysis*. NBS Special Publications, **298**, 133–154.

FRANCIS, D. M. 1976. The origin of amphibole in lherzolite xenoliths from Nunivak Island, Alaska. *Journal of Petrology*, **17**, 357–378.

FREDA, C. & SCARLATO, P. 2001. La diffusione nei fusi silicatici. *Quaderni di Geofisica, Istituto Nazionale di Geofisica e Vulcanologia*, **14**, 1–23.

FREDA, C., BAKER, D. R. & OTTOLINI, L. 2001. Reduction of water loss from gold–palladium capsules during piston-cylinder experiments by use of pyrophyllite powder. *American Mineralogist*, **86**, 234–237.

HIROSE, K. & KAWAMOTO, T. 1995. Hydrous partial melting of lherzolite at 1 GPa: the effect of H_2O on the genesis of basaltic magmas. *Earth and Planetary Science Letters*, **133**, 463–473.

IONOV, D. A., BODINIER, J.-L., MUKASA, S. B. & ZANETTI, A. 2002. Mechanisms and sources of mantle metasomatism: major and trace element composition of peridotite xenoliths from Spitsbergen in the context of numerical modelling. *Journal of Petrology*, **43**, 2219–2259.

IRVING, A. J., HUANG, W. L. & WYLLIE, P. J. 1977. Phase relations of portlandite, calcium hydroxide and brucite, magnesium hydroxide to 33 kilobars. *American Journal of Science*, **277**, 313–321.

KING, P. L., HERVIG, R. L., HOLLOWAY, J. R., DELANEY, J. S. & DYAR, M. D. 2000. Partitioning of Fe^{3+}/Fe_{total} between amphibole and basanitic melt as a function of oxygen fugacity. *Earth and Planetary Science Letters*, **178**, 97–112.

LE BAS, M. J., LE MAITRE, R. W., STRECKEISEN, A. & ZANETTIN, R. 1986. A chemical classification of volcanic rocks based on the total alkali–silica diagram. *Journal of Petrology*, **27**, 745–750.

LUNDSTROM, C. C. 2003. An experimental investigation of diffusive infiltration of alkalis into partially molten peridotite: implications for mantle melting processes. *Geochemistry, Geophysics, Geosystems*, **4**, 1–25.

MATSUKAGE, K. & KUBO, K. 2003. Chromian spinel during melting experiments of dry peridotite (KLB-1) at 1.0–2.5 GPa. *American Mineralogist*, **88**, 1271–1278.

MISITI, V., FREDA, C., TADDEUCCI, J., ROMANO, C., SCARLATO, P., LONGO, A., PAPALE, P. & POE, B. T. 2006. The effect of H_2O on the viscosity of K-trachytic melts at magmatic temperatures. *Chemical Geology*, **235**, 124–137.

MORGAN, Z. & LIANG, Y. 2003. An experimental and numerical study of kinetics of harzburgite reactive dissolution with applications to dunite dike formation. *Earth and Planetary Science Letters*, **214**, 59–74.

MORIMOTO, N. 1989. Nomenclature of pyroxenes. *Canadian Mineralogist*, **27**, 143–156.

NAVON, O. & STOLPER, E. 1987. Geochemical consequence of melt percolation: the upper mantle as chromatographic column. *Journal of Geology*, **95,** 285–307.

NEAL, C. R. 1988. The origin and composition of metasomatic fluids and amphiboles beneath Malaita, Solomon Islands. *Journal of Petrology*, **29**, 149–179.

NIELSEN, R. L. & DRAKE, M. J. 1979. Pyroxene-melt equilibria. *Geochimica et Cosmochimica Acta*, **43**, 1259–1272.

NIIDA, K. & GREEN, D. H. 1999. Stability and chemical composition of pargasitic amphibole in MORB pyrolite under upper mantle conditions. *Contributions to Mineralogy and Petrology*, **135**, 18–40.

O'HARA, M. J. 1968. The bearing of phase equilibria studies in synthetic and natural systems on the origin and evolution of basic and ultrabasic rocks. *Earth-Science Reviews*, **4**, 69–133.

ORLANDO, A. & BORRINI, D. 2001. Solubility of Ti in andradite under upper mantle conditions: preliminary results. *Periodico di Mineralogia*, **70**, 99–110.

ORLANDO, A., ARMIENTI, P., CONTICELLI, S., VAGGELLI, G. & MANETTI, P. 1997. Petrological investigations on the primitive Cainozoic lavas of Northern Victoria Land, Antarctica. *In*: RICCI, C. A. (ed.) *The Antarctic Region: Geological Evolution and Processes*. Terra Antartica Publications, Siena, 523–529.

PERINELLI, C. & ARMIENTI, P. 2005. Pyroxenites and megacrysts in alkaline basaltic magmas from northern Victoria Land (Antarctica): constraint on the thermal evolution of sub-continental lithosphere. *Ofioliti*, **30**, 231.

PERINELLI, C., ARMIENTI, P. & DALLAI, L. 2006. Geochemical and O-isotope constraints on the evolution of lithospheric mantle in the Ross Sea rift area (Antarctica). *Contributions to Mineralogy and Petrology*, **151**, 245–266.

PETERSON, J. W. & NEWTON, R. C. 1990. Experimental biotite-quartz melting in the KMASH-CO_2 system and the role of CO_2 in the petrogenesis of granites and related rocks. *American Mineralogist*, **75**, 1029–1042.

PHILIBERT, J. 1963. A method for calculating the absorption correction in electron probe microanalysis. *In*: PATTEE, H. H., COSSLETT, V. E. & ENGSTRÖM, A. (eds) *X-ray Optics and X-ray Microanalysis*. Academic Press, New York, 379–392.

RAPP, R. P., SHIMIZU, N., BORMAN, M. D. & APPLEGATE, G. S. 1999. Reaction between slab-derived melts and peridotite in the mantle wedge: experimental constraints at 3.8 GPa. *Chemical Geology*, **160**, 335–356.

ROCCHI, S., ARMIENTI, P., DI VINCENZO, G., CARDINI, I., ROSSETTI, F. & STORTI, F. 2006. Tight link between Cenozoic magmatism and local-regional fault activity in the West Antarctic Rift. *Terra Antartica Reports*, **12**, 73–80.

ROCHOLL, A., STEIN, M., MOLZAHN, M., HART, S.R. & WÖRNER, G. 1995. Geochemical evolution of rift magmas by progressive tapping of a stratified mantle source beneath the Ross Rift, Antarctica. *Earth and Planetary Science Letters*, **131**, 207–224.

ROEDER, P. L. & EMSLIE, R. F. 1970. Olivine-liquid equilibrium. *Contribution to Mineralogy and Petrology*, **29**, 275–289.

SEN, C. & DUNN, T. 1994. Experimental modal metasomatism of a spinel lherzolite and the production of amphibole-bearing peridotite. *Contributions to Mineralogy and Petrology*, **119**, 422–432.

SHAW, C. S. J. 1999. Dissolution of orthopyroxene in basanitic magma between 0.4 and 2 GPa: further implications for the origin of Si-rich alkaline glass inclusions in mantle xenoliths. *Contributions to Mineralogy and Petrology*, **135**, 114–132.

SHAW, C. S. J., THIBAULT, Y., EDGAR, A. D. & LLOYD, F. E. 1998. Mechanisms of orthopyroxene dissolution in silica-undersaturated melts at 1 atmosphere and implications for the origin of silica-rich glass in mantle xenoliths. *Contributions to Mineralogy and Petrology*, **132**, 354–370.

SHAW, C. S. J., HEIDELBACH, F. & DINGWELL, D. B. 2006. The origin of reaction textures in mantle peridotite xenoliths from Sal Island, Cape Verde: the case for 'metasomatism' by the host lava. *Contributions to Mineralogy and Petrology*, **151**, 681–697.

ULMER, P. & LUTH, R. W. 1991. The graphite–COH fluid equilibrium in P, T, fO_2 space; an experimental determination to 30 kbar and 1600 °C. *Contributions to Mineralogy and Petrology*, **106**, 265–272.

VAGGELLI, G., OLMI, F. & CONTICELLI, S. 1999. Quantitative electron microprobe analysis of reference silicate mineral and glass samples. *Acta Vulcanologica*, **11**, 297–303.

VERNIÈRES, J., GODARD, M. & BODINIER, J.-L. 1997. A plate model for the simulation of trace element fractionation during partial melting and magma transport in the Earth's upper mantle. *Journal of Geophysical Research*, **102**, 24771–24784.

WALLACE, M. E. & GREEN, D. H. 1991. The efffect of bulk rock composition on the stability of amphibole in the upper mantle: implications for solidus positions and mantle metasomatism. *Mineralogy and Petrology*, **44**, 1–19.

XU, Y. G. & BODINIER, J.-L. 2004. Contrasting enrichments in high- and low-temperature mantle xenoliths from Nushan, Eastern China: results of a single metasomatic event during lithospheric accretion? *Journal of Petrology*, **45**, 321–341.